Rev.Adv.Mater.Sci. 21(2009) 107-133

SIZE-DEPENDENT EFFECTS IN PROPERTIES OF NANOSTRUCTURED MATERIALS

R.A. Andrievski

Institute of Problems of Chemical Physics, Russian Academy of Sciences, Chernogolovka, Moscow Region, 142432, Russia

Received: February 17, 2009

Abstract. Size-dependent effects in nanostructured (nanocrystalline, nanophase or nanocomposite) materials are of great importance both for fundamental considerations and modern technology. The effect of the nanoparticle/nanocrystallite size on surface energy, melting point, phase transformations, and phase equilibriums is considered as applied to nanostructured materials. The role of size-dependent effects in phonon, electronic, superconducting, magnetic, and partly mechanical properties is also analyzed in detail. Special attention is paid to the contribution of other factors such as the grain boundary segregations, interface structure, residual stresses and pores, non-uniform distribution of grain sizes, and so on. The little explored and unresolved problems are pointed and discussed.

1. INTRODUCTION

Size-dependent effects (SDE, i.e. the characteristic size influence of grains, particles, phase inclusions, pores, *etc*., on the properties of materials and substances) have been studied in physics, chemistry, and materials science for a long time. It is quite enough to list the following well-known equations of Laplace, Thomson (Kelvin), Gibbs-Ostwald, Tolman, J. Thomson, Hall-Petch, Nabarro-Herring, and Coble, which connect the capillary pressure (P), saturated vapor pressure (p), saturated solubility (C), surface energy of flat surface (σ_0), conductivity (λ), hardness (H) and creep rate (ε') correspondingly with the pore/inclusion radius (r), thickness film (h) and grains/crystallites size (L):

$$P = 2\sigma_0 / r, \tag{1}$$

$$p(r) = p_0 \exp(2\sigma_0\Omega / rRT), \tag{2}$$

$$C(r) = C_0 \exp(2\sigma_0\Omega / rRT), \tag{3}$$

$$\sigma_0(r) = \sigma_0 / (1 + 2\xi / r), \tag{4}$$

$$\lambda(h) = 0.5\lambda_0 f[\ln(1/f) + 15], \tag{5}$$

$$H(L) = H_0 + AL^{-0.5}, \tag{6}$$

$$\dot{\varepsilon} \sim 1/L^m, \tag{7}$$

where p_0 is the equilibrium pressure of saturated vapor on flat surface, C_0 is the equilibrium solubility of subject with flat surface, Ω is an atomic (molar) volume, R is the gas constant, T is temperature, ξ is the Tolman constant, λ_0 is conductivity of grain-coarse material (thick film), $f = h/l_0$, l_0 is the mean free pass of carriers ($f < 1$), H_0 is the friction stress in the absence of grain boundaries (GB) and A is a constant. The factors m=2 and 3 correspond to the Nabarro-Herring diffusion creep and to the Coble diffusion creep correspondingly.

The development of modern advanced nanostructured materials (NM) manifests some new problems such as the identification adaptability of these equations (1-7) and other those in na-

Corresponding author: R.A. Andrievski, e-mail: ara@icp.ac.ru

nometer interval; the role of quantum effects as well as an influence of other factors in the NM properties or their stability and reproducibility. All these things are very important and actual to consider the SDE features taking in mind the update high rate in this field and not only fundamental considerations, but the strategy optimal development for nanotechnology. These questions have been analyzed early by the present author [1-5] and other investigators (see, e.g., [6-19]). It seems to be necessary to tell apart the SDE in the isolated nanosubjects (clusters, nanoparticles, nanowires, and nanotubes) and consolidated ones (nanobulks, nanocomposites, and nanofilms/nanocoatings). Analyses of SDE in consolidated NM can be found in reviews [1-6], but the most publications were devoted to nanoparticles and clusters. Naturally, the SDE topic as a whole seems not to be covered, because there are many new results scattered throughout the literature.

Taking into account the comprehensive books [9,10,13,15,16], this review is mainly devoted to the SDE recent analysis in consolidated NM (papers mainly from 2001-2002), although some results for isolated nanosubjects will be also considered with the exception of catalytic and biological properties. Moreover, the comprehensive problem on the SDE in mechanical properties will be also discussed in limited scale as applied only to brittle high-melting point compounds (see Section 4 below).

It is important to point that there are at least five principal features of size effects in consolidated NM [1-5]:

- the crystalline size reduction to the nanometer scale results in a significant increase of the role of the interface defects such as GB, triple junctions (TJ), and elastically distorted layers;
- interfacial properties on a nanometer scale can be different from those of conventional grain-coarse materials;
- the reduced crystallite size can be overlapped by characteristic physical lengths such as the mean free path of carriers or the Frank-Read loop size for dislocations and so on;
- size effects in NM can have quantum nature if the crystallite size is commensurable with the De Broyle wavelength $l_B=\hbar/(2m^*E)^{1/2}$ where $\hbar$ is the Planck constant, m^* is the electron effective mass, E is the electron energy. Based on known values of m^* and E, it is possible to predict that the quantum size effects can be exhibited in metals only when the crystallite size is lower than ~ 1 nm. For semiconductors (especially with narrow gap-zone, e.g., InSb) and semimetals (e.g., Bi), the l_B value is significantly higher and can be of about 100 nm;
- unlike conventional grain-coarse materials, in NM there are many factors for masking SDE such as residual stresses, pores, TJ and the presence of other defects, progressive accumulation of interface segregations, non-equilibrium phase appearance, and so on.

All these peculiarities may reveal in the presence of certain specific points in the size dependencies and in the non-monotonous change of the properties determined by decreasing of the grain size. As a rule, such non-monotonous change is especially characteristic for structure-sensitive properties. For example, such specific features, i.e. twist points, and non-monotonous change of properties have been revealed in the known hardness and magnetic coercivity studies (see, e.g., [1,2,4]). Such changes can be connected with different factors such as other mechanisms of SDE, progressive accumulation of segregations on interfaces, and so on.

2. THERMODYNAMIC PROPERTIES

2.1. Surface energy

The problem concerning surface energy is important both for fundamental sense and for many materials science and engineering applications such as the prognosis of phase diagrams, the estimations of the fracture, milling, dilution, wetting, nucleation, coagulation, recrystallization characteristics, and so on. In this connection, the revealing of surface energy change in nanometer interval is of special interest.

Tolman's equation (4), i.e. the effect of the drop radius on surface energy, has been widely discussed (see, e.g., [7,8,11,14,20-23]). Omitting the details of these calculations, which are based on different physical and chemical approaches, let us to consider these results as a whole. Being applied to isolated nanocrystals under calculations [11,14], the amendment $g(r)$ to the conventional σ_0 value fixed on the capillary pressure (1) is described by the following expression

$$g(r) = \left[2\ln(2r) - 1 + 1/4r^2\right] / \left[2r^2 - 2\ln(2r) - 1/8r^2\right]. \quad (8)$$

For many nanocrystals this amendment is very small and comes into particular prominence (about 10%) only at $r < 5$ nm.

The radius effect on surface energy can be also described by equations:

$$\sigma(r) = \begin{cases} Kr \ at \ r < r_0, \\ \sigma_0 \ at \ r > r_0, \end{cases} \quad (9)$$

where K is a constant, r_0 is critical radius (of 2-10 nm) [21]. There are other theoretical calculations that have revealed about the similar values of critical radius lower of which surface energy is decreased (see, e.g., [20,22]). The experimental results in this field are very limited, ambiguous, and often mutually contradictory. From one side, electrochemical measurements have revealed the σ_r values about 0.2 J/m^2 and 0.7 J/m^2 for Ag nanoparticles of r ~ 50 nm and r ~ 150 nm accordingly to [24]. These values seem to be not so precise but are reasonable (it is appropriate to compare them with the value of σ_0 = 1.14 J/m^2 and with the GB energy of ~0.27 J/m^2). From the other side, the experimental study of size-dependent evaporation of free-spherical Ag and PbS nanoparticles using relationship (2) results in values of 7.2 J/m^2 and 2.45 J/m^2 respectively, these values are significantly higher as compared to that of the flat bulks [25]. May be, this is an effect of the evaporation conditions (see Section 2.2) or there is a systematic error in the experimental results [25].

As applied to nanocrystalline solids the analysis of size- or curvature-dependent interface, free energy results to the following relationship

$$\sigma(r) \approx \sigma_0(1 - t / r), \quad (10)$$

where t is an interfacial layer (the semi-width of GB in consolidated nanometals) [7,8]. It is easy to see that at the reasonable values of 2t ~ 1nm and r = 5 nm the σ decreasing is of 10% that is in close agreement with estimations under Eq. (8).

In Debye approximation, the Tolman constant ξ in Eq. (4) can be expressed as

$$\xi = 15h'(\alpha - 1), \quad (11)$$

where h' is the height of atomic monolayer, α is the ratio of root-mean-square amplitude of thermal vibrations of atoms on surface and in volume [23]. If $\alpha > 1$ and $\xi > 0$, then $\sigma_r < \sigma_0$ and in the opposite case $\alpha < 1$ and $\xi < 0$ then $\sigma_r > \sigma_0$. As it will be seen from here on, these two cases are important as applied to the behavior analysis of nanoparticles in matrices.

It is known that distinct feature of nanostructure in NM is that, with the grain size confinement, the part of TJ is increased and, accordingly, the part of GB is decreased (see, e.g., [4]). The computer modeling with account of GB and TJ contributions reveals that Ni grain size reducing is accompanied by decrease of the total excess enthalpy (i.e. the total GB energy) [26]; this result quantitatively agrees with experimental data for nano Se [27].

The calculated interface GB energy in Cu-Ni bilayered nanofilm changes from 0.9 J/m^2 to about 0.7 J/m^2 when bilayer thickness decreases from ~1 nm to ~0.4 nm [28].

From the foregoing data it has been evident that in spite of different theoretical approaches in calculations, they are evidence of the σ decrease in the confinement of isolated nanosubjects and nanostructures in NM. It seems to be reasonable to introduce the amendments into grain/crystalline boundary energy values at L lower than near 10 nm. However, it is also evident that experimental studies in this field are necessary for further detailed continuation.

The comprehensive description of the SDE role in the other surface phenomena such as wetting, nucleation, adsorption, and capillarity can be found in book [16]. It is worth to note that the observation by high-resolution transmission electron microscope (HRTEM) methods is in common practice (see, e.g., [19,29,30]).

2.2. Melting point

It is well known for a long time that small particles and thin films are characterized by the lower melting points (T_m) as compared with their counterparts in bulk form as a result of the atom thermal vibration amplitude increase in the surface layers. There are many relationships contacting T_m and r for free-standing (supporting) metal (Au, Ag, Cu, Sn, *etc*.) clusters/nanoparticles as well as h for thin films (see, e.g., [4,10,13,15,16,19]). Generally, all proposed equations have the form of $T_m \sim 1/r(h)$ type.

Recent theoretical and experimental works tend to obtain more precise specifications: the size, shape, and stress effects on the T_m nanograins on a substrate [31]; the role of fractal structure [32]; the comparison of SDE in the case of spherical nanoparticles, nanofilms, and nanowires [9,33]; the effect of transition to amorphous state [34], kinetic study of the Cu film melting-dispergation [35], *etc*. Thus the consideration of size-dependent cohesive energy results in the T_m variation for spherical nanoparticle, nanowire, and nanofilm of a material in the same characteristic size as 3:2:1 that is confirmed by experimental values for In [33]. The molecular dynamics simulation of the melting behavior for "model" nanocrystalline Ag has exhibited two characteristic regions on the grain size decrease [34]. The first is above about 4 nm where the T_m

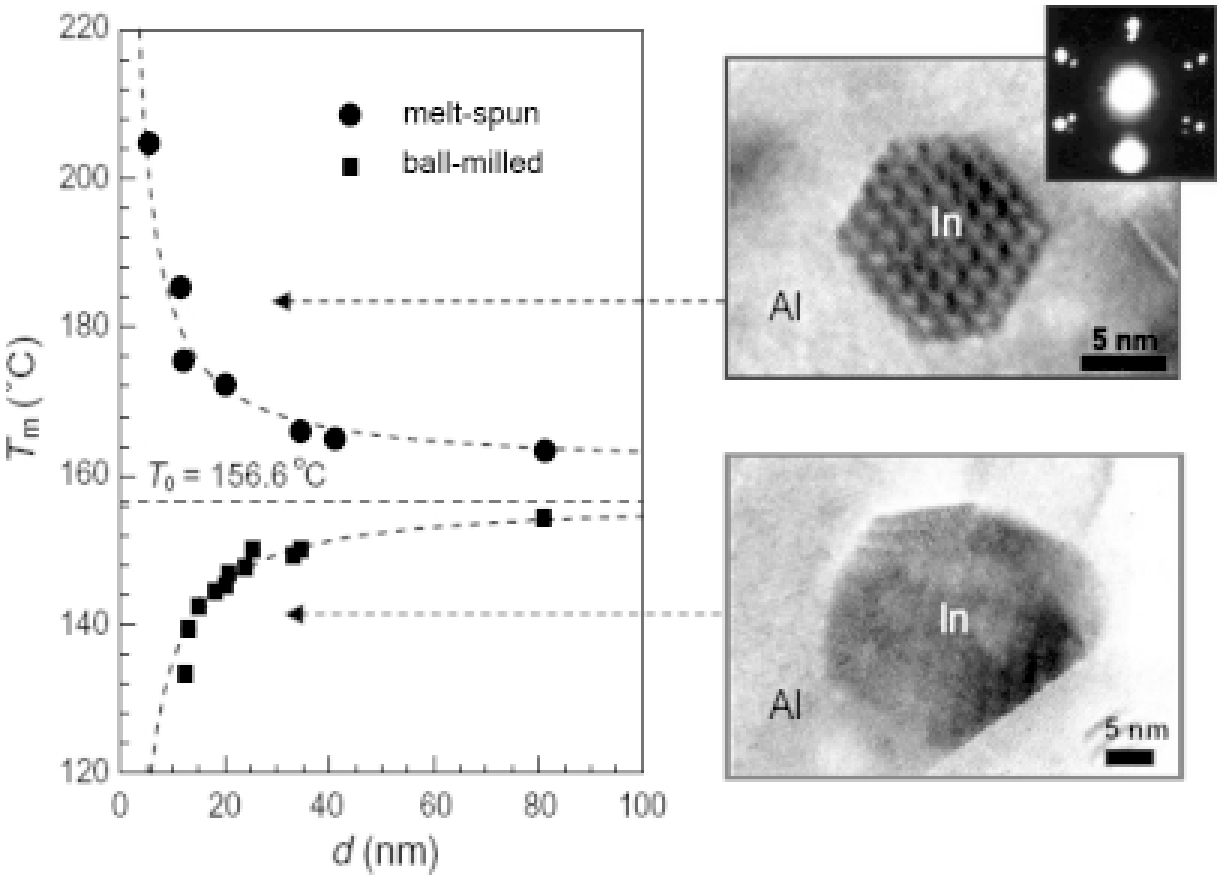

Fig. 1. Melting point of In nanoparticles embedded in Al matrix for two methods of preparation as a function of particle diameter: ball milling (■) and spinning (●). HRTEM images illustrated the different In/Al interface structures, replotted from [19].

values decrease with grain size decreasing. The second one (r < 4 nm) is a size-independent region where the T_m values almost keep a constant. The dominant factor in this situation is supposed to be the nanocrystal T_m shifts from grain to GB. The amorphous phase (r < 1.3 nm), as indicated from the radial distribution function and common neighbor analysis, is different from the GB by the sharp enhancement of local fivefold symmetry and is characterized by a much lower solid-to-liquid transformation temperature than that of Ag nanocrystal and GB. Melting and non-melting of solid surfaces including partly behavior of nanosystems are discussed in review [12].

When the nanosolids are entirely coated by a high-melting point substance or embedded in such matrix, the nanosolid T_m values can not only decrease but increase too; this interesting phenomena is named by superheating or overheating. The SME detailed analysis at melting and superheating of bulks and nanosolids can be found in review [19]. The crucial role of interface in superheating is clearly demonstrated by the measurement results of the ball-milled and the melt-spun Al-In samples T_m values as a function of particle size of In (Fig. 1) [19].

Fig. 1 clearly demonstrates that samples prepared by the two methods undergo completely different melting behaviors which were investigated using differential scanning calorimetry (DSC), in-situ HRTEM, and in-situ X-ray diffraction (XRD). In the case of ball-milling procedure, there are irregular In particles and the incoherent random interfaces were formed between particles and the matrix, then the nanoparticles exhibit the SDE T_m depression, as described previously. In the case of melt-spun samples, the In particles were found to be distributed both in the Al GB and within the Al grains. The particles within Al grains are truncated by octahedral shapes bounded by {111}/(100) fac-

Table 1. Structure of unusual phases observed in some NM [37].

Compound (metal, alloy)	Usual bulk phase at *RT* and $P=10^6$ Pa	Observed nanocrystalline phase
ZrO_2	Monoclinic	Tetragonal
$BaTiO_3$	Cubic	Tetragonal
$PbTiO_3$	Cubic	Tetragonal
Al_2O_3	α-Al_2O_3	γ-Al_2O_3
TiO_2	Rutile	Anatase
Y_2O_3	Cubic (α-Y_2O_3)	Monoclinic (γ-Y_2O_3)
CdSe, CdS	Wurtzite	Rock salt
Co	*hcp** (α-Co)	*fcc** (β-Co)
T	*hcp* (α-Ti)	*bcc** (β-Ti)
Fe-Ni	Martensite	Austenite (fcc)

**hcp* is hexagonal-closed-packed structure; *fcc* is face-centered-cubic structure; *bcc* is body-centered-cubic structure.

ets and can be considered as epitaxial coherent interfaces revealing the T_m increase with decreasing of r. It is interesting to know whether other properties, not only melting point, are also changing under the ball-milled and melt-spun nanoparicles in matrices. The superheating has been also observed in the systems of Pb-Al and Ag-Ni both in the Al and Ni matrixes as well as partly in layered Pb/Al films [19].

On phenomenological level, superheating is explained by change of root-mean-square amplitude of thermal vibrations of atoms on surface and in volume (Eq. (11) [23]) and by modification of interfacial energy [19] or the coherent interface parameter between inclusions and matrix [36].

2.3. Phase transformations

Apart of melting point SDE make an impact on other phase transformations in NM. Table 1 summarizes some data in this field [37].

Observed solid-state transformations are considered to be connected with an increased effective internal pressure due to high surface/interfacial curvature or with the whole and surface energy difference between allotropic phases [37]. The tetragonal-to-monoclinic (T $\rightarrow$ M) phase transformation in the zirconia-yttria system is the most explored subject. Fig. 2 shows experimental data on the T $\rightarrow$ M transformation temperature (T_{tr}) for different YSZ powders and sintered pellets with particles/grains in the nanometer interval [38].

In Fig. 2 each line demarcated the tetragonal phase stability region (defined as “T”) and that to left of the line (defined as “T+M”) where the T-phase starts to transform into the M-phase which was fixed in both the DSC and the dilatometer studies. It is evident from these results that the T_{tr} value is decreased with a reduction of crystallite/grain size. The curve extrapolation provide the opportunity to predict the particle critical size values at room temperature of the T-phase stability: 15, 30, 51, and 71 nm for 0YSZ, 0.5YSZ, 1.0YSZ, and 1.5YSZ powders, respectively. In the case of the 0.5YSZ, 1.0YSZ, and 1.5YSZ sintered pellets, the grain critical size values are 70, 100, and 155 nm, respectively. The observed difference in crystalline/grain size (about 2 times) can be attributed to the strain energy term and difference in the surface and interfacial energies.

In the thermodynamic approach frame, the following relationships between the T_{tr} value and critical crystalline/grain size (D_c, L_c) have been proposed

$$1/D_c = \Delta H_b\left(1 - T_{tr}/T_b\right)/\left(6\Delta\sigma\right) \quad \text{(for powders)}, \tag{12}$$

$$1/L_c = \Delta H_b\left(1 - T_{tr}/T_b\right)/\left(6\Delta\Sigma\right) + \Delta U_d/6\Delta\Sigma \quad \text{(for pellets)}, \tag{13}$$

where ΔH_b and T_b are the enthalpy and transformation temperature for bulk (coarse-grained) solids, $\Delta\sigma$ and $\Delta\Sigma$ are the differences in the surface/interfacial energies for T/M phases in powders and pellets, ΔU_d is the strain energy involved in the transformation (this additional strain-energy term estimates only for consolidated pellets) [37,38].

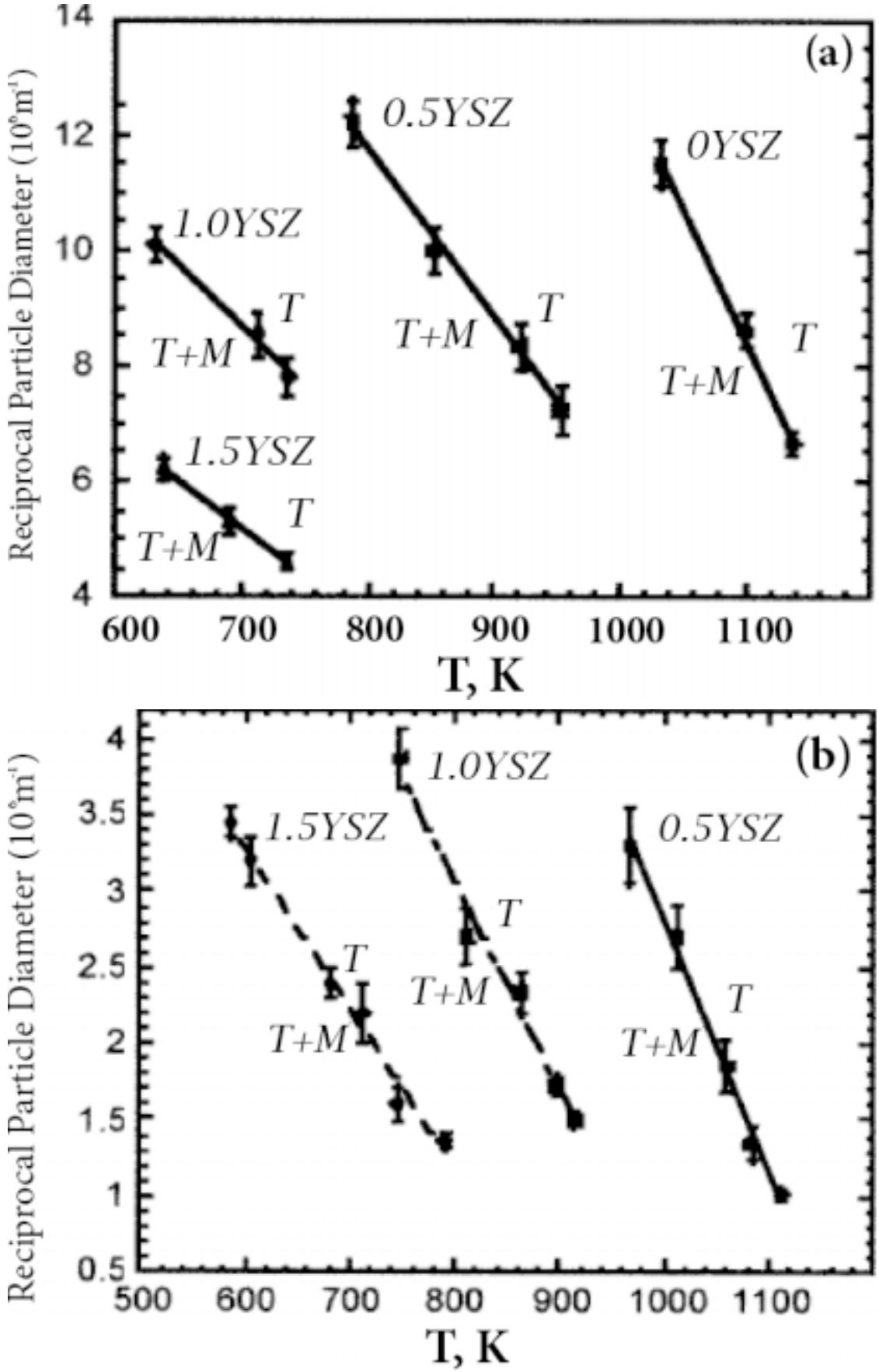

Fig. 2. Inverse critical grain/crystalline size versus transformation temperature (T → M) for different yttria-doped zirconia (a) powders and (b) pellets: 0YSZ – pure ZrO_2, 0.5YSZ – 0.5 mol.%Y_2O_3, 1.0YSZ – 1.0 mol.%Y_2O_3, 1.5YSZ – 1.5 mol.%Y_2O_3, replotted from [38].

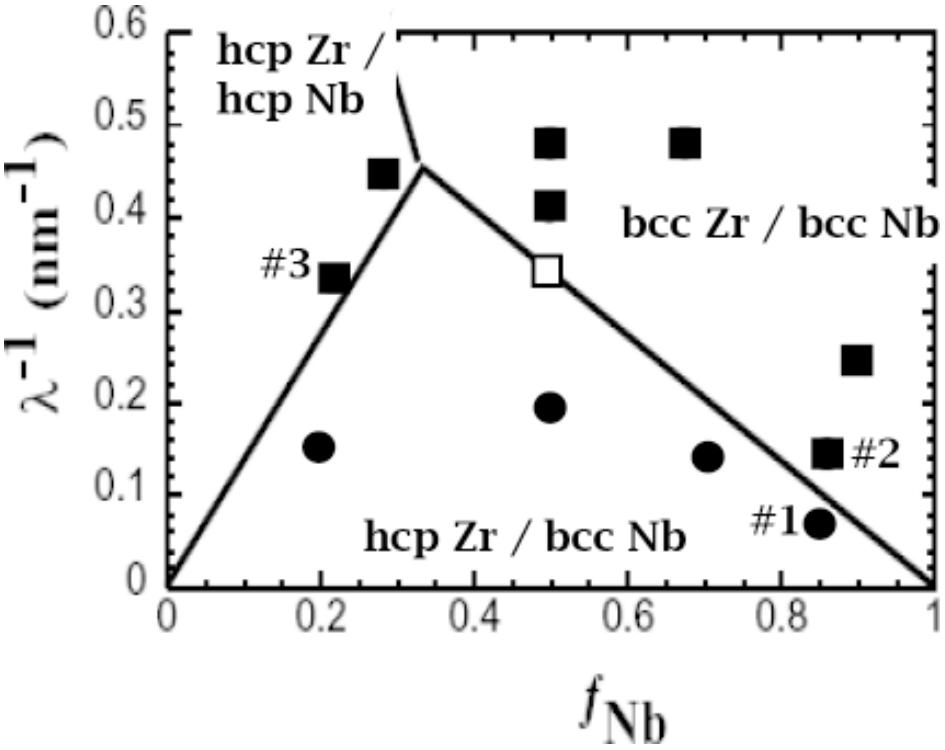

Fig. 3. The phase stability diagram for Nb/Zr multilayers as a function of the Nb volume fraction (f_{NB}) and the inverse of bilayer thickness (λ^{-1}): # 1 is the stability region of *hcp*Zr/*bcc*Nb; # 2 is the stability region of *bcc*Zr/*bcc*Nb; # 3 is the stability region of *hcp*Zr/*hcp*Nb. The circles indicate experimental results and the line boundary calculated from the thermodynamic model, replotted from [41].

The possibility to observe also the high-temperature phase at low temperature is the situation when the elementary crystal (germ) size of this phase is lower than crystallite size. Such situation tends to the transformation blocking and the high-temperature phase is fixing. This example is typical for some martensite transformations in the Fe-Ni and Ti-Ni-Co micro- and nanocrystalline alloys [39]. The martensite volume part (M) depends on the high-temperature initial phase crystallite size under the equation

$$M = M_0 - K_m L^{-0.5}, \qquad (14)$$

where M_o and K_m are some constants. The relationship (14) coincides with that of Hall-Petch one (6). This agreement could be connected with the analogous nature of elastic strain fields at the crack and germ propagation.

The availability of non-equilibrium phases in thin film is observed for a long time. Under film thickness lower than some critical value (h_c), non-common phases can be fixed; that is connected with the Gibbs free energy excess effect due to the surface effect. One of the first relationships describing this effect was proposed more than 50 years ago

$$h_c = (\sigma_1 - \sigma_2) / (F_2 - F_1), \qquad (15)$$

where indexes 1 and 2 correspond to equilibrium and non-equilibrium phases, respectively, σ_i and F_i are the total surface energy and the Gibbs free energy of these phases [40]. The h_c rough estimation by Eq. (15) resulted in the quite reasonable values (h_c ~ 10 nm).

Basically, the idea [40] based on a classical thermodynamic approach with some modifications is used in many modern studies especially with the development of nanostructured thin film multilayers such as Ti/Al(Nb, Zr) and TiN/AlN(NbN, ZrN), Fe/Cr, *etc*., which can exhibit metastable structures in one or both layers. Fig. 3 shows the phase stability diagram for Nb/Zr multilayers with varying volume fractions and bilayer ($\lambda_{Nb} + \lambda_{Zr}$) thickness [41].

The phase stability region boundaries were calculated using a classical thermodynamic model taking into account the structural energy assess-

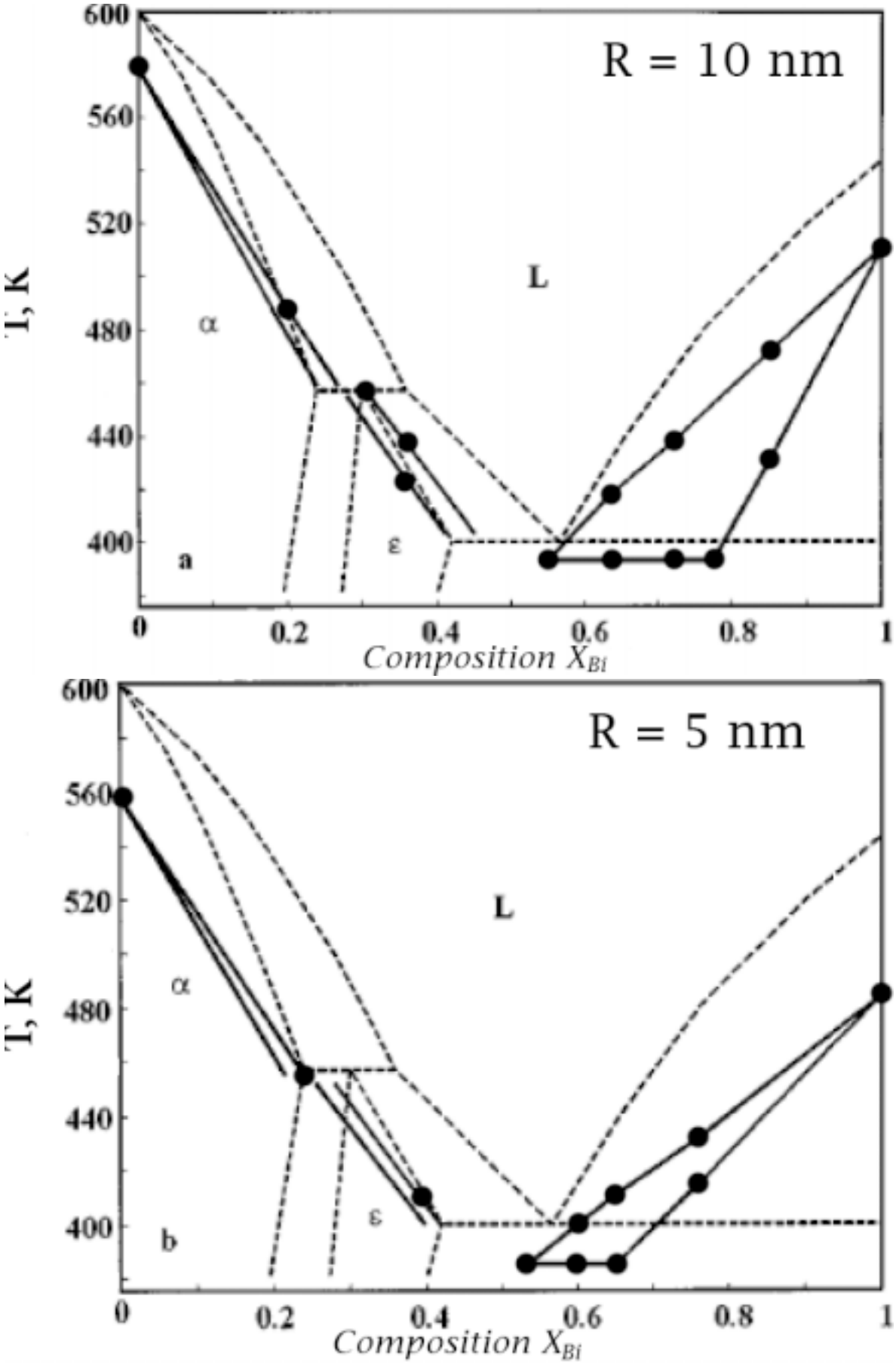

Fig. 4. The Bi-Pb phase diagram. The dashed lines are the equilibrium bulk phase diagram and the solid lines are experimental results for nanoparticles of (a) 10 nm radii and (b) 5 nm radii, replotted from [42].

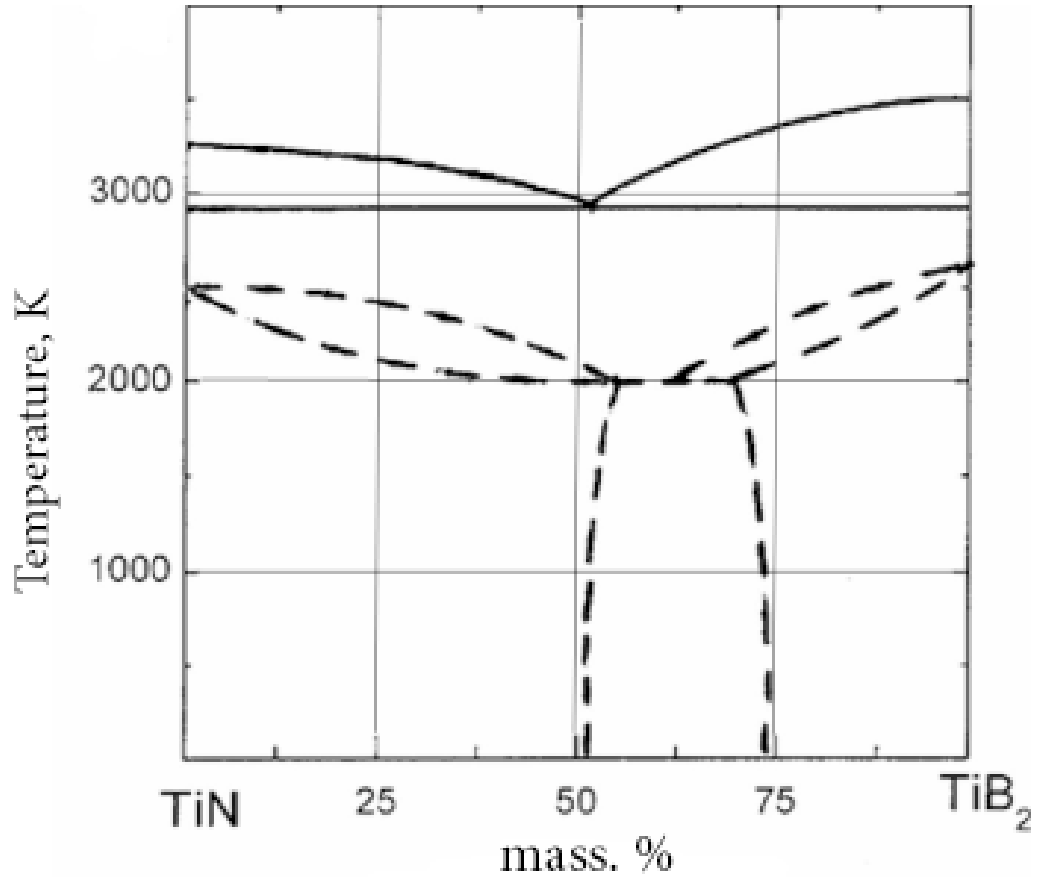

Fig. 5. Pseudobinary TiN-TiB_2 phase diagram for equilibrium state (the solid lines) and for nanostructured films (L ~ 10 nm), replotted from [44].

ment in the interfacial energy value. The equilibrium phases (*hcp* Zr and *bcc* Nb) were observed only in the region #1; at that, the effect of the Nb volume fraction is not monotonous. The presence of the non-equilibrium *bcc* Zr and *hcp* Nb phases in sputtered films (regions #2 and #3, respectively) was confirmed experimentally by XRD and electron diffraction.

2.4. Phase equilibriums

By now there are several examples of theoretical calculations and experimental studies of the phase diagram SDE in nanointerval: ZrO_2-Y_2O_3 [37], Pb-Bi [42], In-Sn [30], Au-Sn [30], carbon phase diagram [43], Al-Pb [18], Bi-Cd [18], TiB_2-TiN [44], TiB_2-B_4C [45], hydrogen systems [46,47], *etc*. Fig. 2 data have been used for the T/T+M line design in the ZrO_2-Y_2O_3 diagram as a function of particle size [37].

The most detailed study was undertaken in the Pb-Bi diagram observing in-situ the melting behavior of isolated alloyed nanoparticles by hot stage TEM. Fig. 4 compares this diagram for particles of 10 nm radii and 5 nm radii as well as for bulks [42].

As shown in Fig. 4, T_m is a size-depend decreasing from the bulk value. The progressive narrowing of two-phase fields and an increase of solubility are also observed. The theoretical calculations developed from thermodynamic first principles were in agreement with experimental results.

The significant increase of solubility for nanosized subjects was observed in many cases including the hydrogen-metal (intermetallic) systems [46,47], Pb-Fe and Pb-Sn systems [48,49], and systems-based high-melting point compounds [44,45]. Fig. 5 shows the TiN- TiB_2 phase diagram both in equilibrium state and film one (the grain size about of 10 nm) [44].

The significant increase in solubility was fixed by the experimental XRD test [50] and the eutectic temperature decrease that was calculated in the regular solution approximation using the phase equilibrium at the eutectic temperature. The con-

tribution made by the surface energy excess for solid state was written in per mole terms as $\Delta F^S = 6V\sigma_{gb}/L$ where V is the molar volume and σ_{gb} is the interfacial (grain boundary) energy (see also [51]). The same approach was used for the SDE analysis in the case of the TiB_2-B_4C phase diagram [45]. Unfortunately, the σ_{gb} value information is very limited. It was supposed in the TiN-TiB_2 phase diagram calculations (Fig. 5) that σ_{gb} ~ 3 J/m^2; in the case of the TiB_2-B_4C phase diagram the more reasonable σ_{gb} interval from 1 J/m^2 to 3 J/m^2 was used[45].

The solubility features in nanosystems are theoretically discussed in papers [52,53]. In many cases, the great role of the grain boundary segregations is pointed (see, e.g., [48]). However, as a whole, the question on the oversaturated solution formation nature remains insufficiently explored as applied to mechanical alloying, ion plating, severe plastic deformation, electrodeposition, and other preparation methods of NM.

Another interesting feature in the SDE on phase equilibriums is that the spinodal decomposition and the triple point coordinates. It was theoretically shown that the grain segregations (thickness of about 1 nm) increase the solid solution decomposition degree when the grain size does not exceed 10 nm [54]. The spinodal decomposition regularities of supersaturated TiN-AlN system with the thermal stable nanostructure formation are very interesting and important for the development of new advanced NM. *Ab initio* calculations revealed the contribution role of strain and surface energy on the energetic balance for decomposition process [55].

The calculation of SDE on the carbon diagram results in the following data for the triple point coordinates defined regions for solid nanodiamond, liquid that and amorphous nanocarbon [43]

Particle diameter, (nm)	1	1.2	1.5	2	3	4	6	Single crystal
Pressure (GPa)	15.2	16.5	16.1	15.6	15.2	14.8	14.5	13.5
T, K	2210	3160	3550	3820	4090	4190	4300	4470

These results are in qualitative agreement with some experimental/theoretical information [56]. The movement of triple point, defined equilibrium between solid state, liquid one, and vapor one, to the temperature decrease and pressure increase with the particle decrease was also described in book [9].

In the most cited works dedicated to the SDE in phase equilibriums, the conditional thermodynamic approaches were used and the interface structure influence was not analyzed. In mean time, as it was shown at the Fig. 1, the impact of external interfaces on T_m can be very great and opposite, so that interface contributions to the thermodynamic functions become significant [18,19]. The analysis of two-phase equilibrium in alloy nanoparticles has revealed the possibility of the eutectic point degeneration into intervals of composition where the alloy melts discontinuously and of the phase diagram topology dramatic changes [57]. These observations tended to conclusion that the concept of equilibrium in nanostructures yet remains to be understood and needs in further detailed study [18,51].

3. PHYSICAL PROPERTIES

3.1. Phonon and electronic properties. Superconductivity

Measurements of electronic heat capacity (γ_e) of Cu-Nb (Pb) nanocomposites and studies of their phonon spectra revealed the decrease of the electronic state density at the Fermi level N (E_F) and the increase of low-frequency oscillations as compared with their coarse-grained (*cg*) counterparts [58,59]. The γ_e value for Nb inclusions (L~20 nm) in $Cu_{90}Nb_{10}$ nanocomposite was of 3.0 mJ/mol K^2 that is about three times lower than that in conventional Nb. The Debye temperature (Θ_D) value is also reduced with the inclusion decrease. These changes were connected with the weakening of interatomic interactions at the GB and assisted by the superconducting transition temperature (T_C) decrease.

The size dependence of T_C, the residual resistance ratio (RRR), the upper critical magnetic field (H_{C2}) and the Ginzburg-Landau coherence length (ξ_{GL}) for the nanocrystalline Nb films are shown in Table 2 [60,61].

It is clear from Table 2 that while the T_C and RRR values decrease with size monotonically, the H_{C2} and ξ_{GL} values increase with size but there is non-monotonous change. The first change is supposed to be connected with the $N(E_F)$ decrease rather than by phonon softening, i.e. the effect of the electron-phonon

Table 2. Grain-size effect of various superconducting and normal-state properties of nanostructured Nb film [60,61].

L (nm)	T_C (K)	$\rho_{300K}/\rho_{10\,K}$ (RRR)	H_{C2} (T)	ξ_{GL} (nm)
60	9.4	8.4	2.8	10.8
50	9.4	6.4	2.8	10.8
28	9.2	4.2	3.4	9.8
19	7.8	2.3	6.6	7.03
17	7.2	1.88	5.1	8.03
11	5.9	1.49	5.1	8.06
<8	no T_C up to 1.76K			

Table 3. Electrical properties of macro – and nanocrystalline oxides.

Oxide	Grain size, (nm)	T, (K)	Conductivity, ($Ohm^{-1}cm^{-1}$)	Activation energy, (eV)
TiO_2 (rutile) [65]	50	713	$4\ 10^{-3}$	0.96
	260	713	$1.4\ 10^{-6}$	1.23
3YSZ* [66]	40	823	$8\ 10^{-4}$	1.04
	1330	823	$1.5\ 10^{-3}$	0.83
10 YSZ* [67]	15	873	10^{-1}	0.62
	Single crystal	873	$6\ 10^{-3}$	1.04
CeO_{2-x} [68]	10	773	$(1\text{-}6)\ 10^{-5}$	0.99
	5000	773	$2.5\ 10^{-7}$	2.45

* ZrO_2+3 mol.% Y_2O_3; ZrO_2+10 mol.% Y_2O_3

coupling is negligible in nano-Nb. The RRR decrease is explained by progressive carriers scattering on the GB, i.e. the mean free path is decreased with size. The H_{C2} non monotonous change is also proposed to reflect competing two opposite effects of the $N(E_F)$ and the mean free path reduction. The first effect tends to reduce H_{C2} and the second results in the H_{C2} increase. The H_{C2} enhancement with the grain size reducing was also observed in the case of other type II nanosuperconductors such as some high-melting point compounds (nitrides, nitrides/carbides, silicides, and so on). Fig. 6 demonstrates the SDE on the H_{C2} value for these compounds; as it is evident the H_{C2} increase can be of about 3 times [62]).

The SDE theory as applied to superconductivity in NM is also discussed and proposed in many works (see, e.g., [17,63,64]). Most calculations based on relationships of $T_C \sim \Theta_D$ and $T_C \sim N(E_F)$ type predict the T_C suppression with size that it is confirmed by experimental data on Nb, MgB_2, Pb, and Bi thin films as well as Pb nanoparticles. Theoretical prediction on the T_C increase [63] is approved only in the case of Al thin films and nanoparticles. This observation is worthy of additional notice.

3.2. Electrical and thermal properties

It is well known that ionic solids are characterized by the complex interface nature. The transition from *cg* bulks to nanostructured subjects is accompanied by the conductivity significant change. Table 3 shows the electrical properties of some oxides with different grain sizes [65-67].

It is evident that the decrease in grain size with the exception of 3YSZ nanosubject is assisted by the increase in conductivity and the decrease in the carrier activation energy. Such difference is connected with the GB space charge potential and the oxygen vacancy concentration. In the case of stabilized Zirconia samples containing 3 mol.% of Y_2O_3, the specific GB conductivity is ~ 2 orders of magnitude lower than the bulk conductivity [66]. It was found that the space charge potential de-

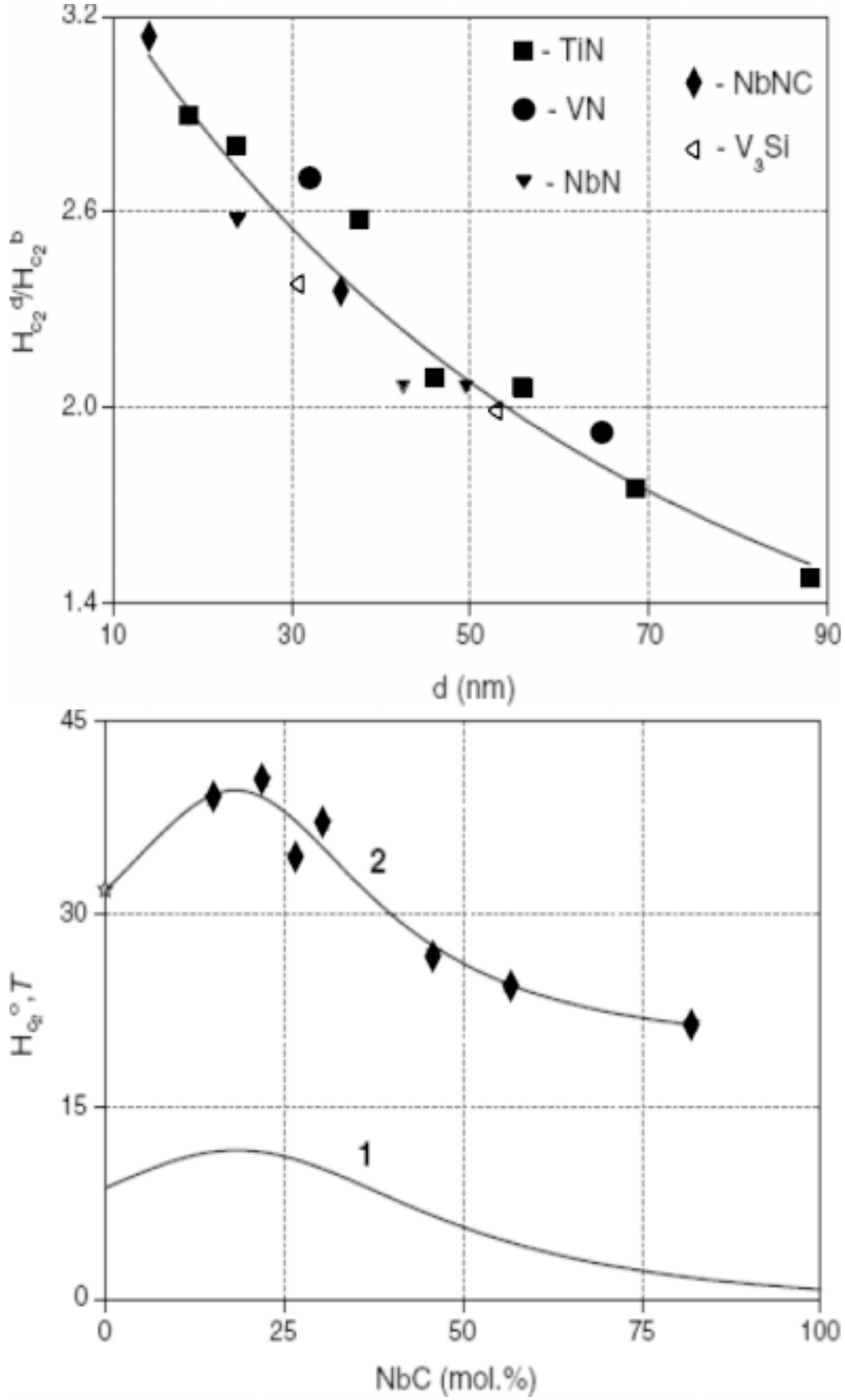

Fig. 6. The grain size effect on the H_{C2} increase: a – H_{C2}^{d} – the critical magnetic field for the TiN, NbN, VN, NbNC, and V_3Si nanopowders; H_{C2}^{b} – the critical magnetic field for the same grain-coarse powders; b – the H_{C2}^{d} and H_{C2}^{b} change for nanoparticles (2) and grain-coarse powders (1) in the NbN-NbC system, replotted from [62].

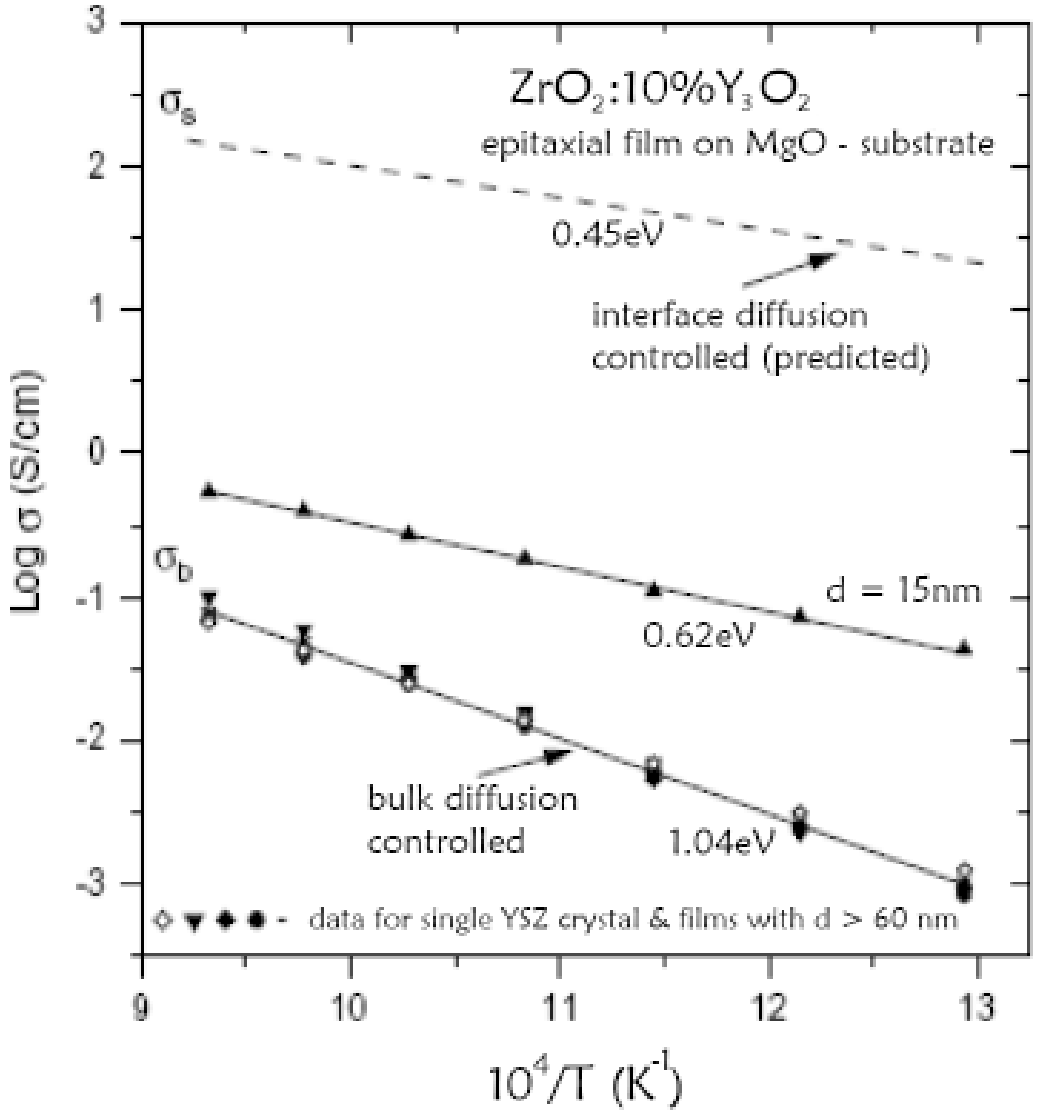

Fig. 7. Temperature dependence of bulk – and interface-limited electrical conductivities for 10YSZ bulks, thin films, and interfaces (calculated results), replotted from [67].

creased, whereas the oxygen vacancy concentration decreased with decreasing grain size in 3YSZ. However, in the case of ultra thin, highly texturing 10YSZ films synthesized on MgO substrates by pulsed laser ablation, the significant interfacial conductivity has been observed [67]. Fig. 7 clearly demonstrates that the interface conductivity, in contrast to statements [66], is about three to four orders of magnitude larger than that of the bulk and its activation energy of 0.45 eV is about half that of the bulk; at that, the experimental results for film with thickness of 15 nm are between bulk and interface data [67].

The data [67] correlate well with the enhancement in the GB oxygen diffusivity which was reported to be more that three orders of magnitude greater than the diffusivity in single crystals [69]. It seems to be reasonable to propose that difference of opinions [66,67] is attributed to the different grain and triple point segregations as soon as their space charge potentials in 3YSZ and 10YSZ.

The theoretical calculations of the energy activation conductivity (Q) decrease in the 16YSZ thin films result in the following relationship

$$Q = Q_0 - (4\lambda\nu / L)\,\mathrm{cth}(4\lambda\nu / LkT), \qquad (16)$$

where Q_O is the energy activation conductivity in single crystal, ν is the volume of oxygen vacancy, λ is electrical conductivity [70]. The relationship (16) was received in the assumption of great effect of

Table 4. Electrical and galvano-magnetic characteristics of TiN films (T = 300 K) [75].

Sample type	Grain size, (nm)	Conductivity, (Ohm^{-1} cm^{-1})	Hall coefficient R_H, (cm^3/C)	Carrier density n, (cm^{-3})	Carrier mobility μ, (cm^2/V s)
Film I	29±15	250	$-2.6\ 10^{-4}$	$2.5\ 10^{22}$	0.065
Film II	8.8±2.2	250	$-2.6\ 10^{-4}$	$2.5\ 10^{22}$	0.007

Table 5. Power factor, thermal conductivity and thermoelectric figure-of-merit of superlattices with high ZT to those of the corresponding bulk materials [77].

Characteristic	PbTe/PbSeTe quantum-dot superlattices	PbTe-PbSeTe bulk alloy	Bi_2Te_3/Sb_2Te_3 superlattices	Bi_2Te_3-Sb_2Te_3 bulk alloys
Power factor ($mW\ cm^{-1}\ K^{-2}$)	32	28	40	50.9
Conductivity ($W\ m^{-1}\ K^{-1}$)	0.6	2.5	0.5	1.26
Thermoelectric figure-of-merit (K^{-1})	5.33	1.12	8	4.04

the Laplace pressure (Eq. (1)) nascent for the nanograin significant curvature effect on the diffusion of oxygen vacancies. The comparison of relationship (16) with experimental results revealed the good coincidence; at that, it was pointed that the main contribution in the conductivity increase can be attributed to the influence interfaces.

The nanowire studies increase the interest to their electrical properties (see, e.g., [71-74]). The temperature effect measurement on the Bi nanowire electrical resistivity revealed a semiconducting behavior with an energy band gap at the critical dimension of less than 50 nm. As applied to the metal-like region, the SDE on the Bi nanowire electrical resistivity (T=300K) wide can be shown as follows [71]:

width of rectangular cross section, (nm)	70	120	200
electrical resistivity (mΩcm)	4.05	2.87	2.30

The Bi electron mean free pass value is about 100 nm and the discussion has indicated that the observed electrical resistivity increase is dominated mainly with grain boundary scattering and carrier scattering at the wire surface plays a secondary role.

Electron scattering at the GB is also found to be a main governing factor for the thermopower SDE for 30 nm Ni nanowires at T > 100K [74]. In this region the thermopower of Ni nanowire is higher than the bulk value. At low temperatures (T < 50K) boundary scattering of phonons inhibits any phonon drag effect that it is in contrast to bulk Ni.

In films-based nitrides, carbides, and borides, there are usually some oxygen contaminations and it is interesting to estimate their distribution, especially in the case of described nanostructured films. The common knowledge is that the measurement of galvano-magnetic properties (such as the Hall coefficient and conductivity) allows to estimate the carrier concentration and mobility. It is also known that these characteristics for nitrides, carbides, oxides, and borides are different. Table 4 summarizes the main results of the conductivity and Hall coefficient on TiN nanofilms, including the charge carrier density n and the mobility μ, estimated from the well-known relations valid in the single-band approximation $R_H = -1/en$ and $\lambda = en\mu$, where R_H is the Hall coefficient, λ is the electrical conductivity, and e is the electron charge [75].

Judging the sign of R_H results to the statement that the major charge of carriers in the samples studied are electrons. The R_H values are also the same in the films of types I and II, i.e. the carrier

density in these films in spite of different grain size is similar. The difference in the film conductivity is connected only with carrier mobility. These films contain a significant amount of oxygen and carbon admixture which could enrich the near-boundary regions and change the carrier density. However, despite of significant difference in the fracture of grain size (and correspondingly in the near-boundary region fracture), the carrier density is the same and then the oxygen and carbon distributions can be considered as random ones in these type I and II films.

With the grain size decrease, the NM thermal conductivity is also reduced as a result of the phonon GB scattering; this can be demonstrated by the example of diamond films and YSZ nanocoatings [4]. The *L* value decrease from 100 nm to 10 nm resulted in the χ value reducing to approximately half of that for coarse-grained or single-crystal specimens of (8-15)YSZ [76].

The possibility to regulate the electrical and thermal conductivity due to nanostructure is very important in the development of new thermoelectric materials. Table 5 compares the main properties of two semiconductor superlattices: the thermal conductivity (χ), the power factor ($S^2\lambda$, where *S* is the thermo power and λ is the electrical conductivity) and the thermoelectric figure-of-merit ($Z = S^2\lambda/\chi$) [77].

The *ZT* value is considered as the main theoretical efficiency of thermoelectric coolers or power generators. It is well known that a high Seebeck coefficient tends to the thermal energy increase (carried per electron or hole). On the other hand, the high electrical conductivity is desirable to minimize the Joule heating losses while the low thermal conductivity value results in the minimization of parasitic heat leakage between the hot and the cold sides. The *ZT* value is also important for the energy conversion by thermo-photovoltaics devices [77]. As can be seen from Table 5, the use of semiconductors–based superlattices (periodic thin film structures) and quantum dots (small nanoinclusions similar to isolated atoms) is very promising for the *ZT* value increase as a result of quantum size effects on carriers and classic interface scattering of phonons.

The further development of the perovskite ferroelectric and granulated nanosolids theory has been developed in many works (see, e.g., some recent papers [78-80]). Such questions as size and interface effects on Curie temperature, conductivity, and dielectric constants were discussed and some relationships were proposed as applied to $BaTiO_3$, $PbTiO_3$, Pt/SiO_2, and $W(Au)/Al_2O_3$ nanoparticles and thin films.

3.4. Magnetic properties

Magnetic characteristics of NM are of great interest for the development of new both hard/soft high efficiency materials and for highly sensitive various sensor devices as well as for high-density numerous data-storage applications. As in the case of mechanical properties, magnetic characteristics depend not only on grain size but on many other factors such as the GB state, texture, residual stresses, and so on. So the SDE role in separation needs in the careful discussion. In this connection, the film studies are enlarged because these nanosubjects allow to understand the nanostructure and properties peculiarities in a deeper level, not to say on the film wide application (see, e.g., [81-86]). The correlation analysis between magnetic properties and nanostructure of films was fulfilled by authors of [81,83].

The coercivity (H_C) and the saturation magnetization (M_S) study of nanocrystalline Ni films with grain sizes in the range of 3-10 nm suggests that the H_C enhancement arises with the *L* values decrease while the M_S decrease is also observed [82]. It is supposed that the first change is a result of the intergrain interaction that is inversely proportional to grain size. The next probable explanation is that the M_S reduction results from the weak interspin interaction due to the coordination number imperfection of atoms near interfaces and the increase of lower-coordinated atoms.

The magnetic properties and nanostructure evolution of the UN thin film were studied in detail [85] for the different deposition temperatures (T = 73-673K). It was observed that the *L* value is about of 17 nm at the low deposition temperature and there are the significant compressive residual stresses and a high density of structure defects (i.e. a very high microstrains) as well as the most pronounced preferential orientation {111}. At the elevated deposition temperatures, this preferential orientation becomes to moderate one and the residual stresses were partly relaxed with the structure defect density decrease. It is pointed that the antiferromagnetism of bulk UN (i.e. the 5f band magnetism) is suppressed and transforms in the weak Pauli paramagnetic behavior in the nanocrystalline state.

An interesting change in magnetic properties has been observed in Fe/Zr multilayers [84]. Fig. 8 shows the Fe sublayer thickness effect on the co-

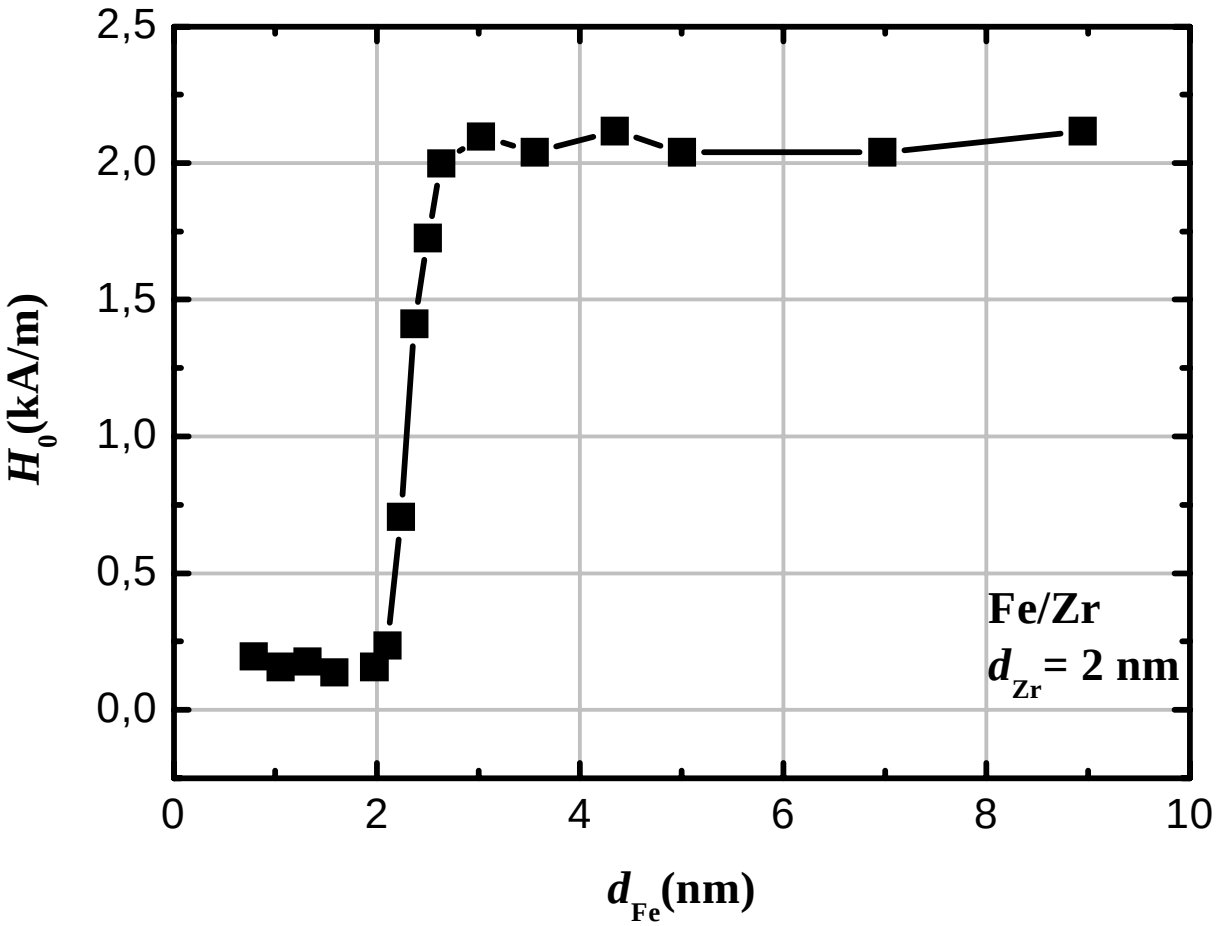

Fig. 8. The coercivity (H_C) as a function of Fe sublayer thickness for wedged Fe/Zr multilayers with the constant Zr layer thickness of 2 nm, data from [84].

ercivity for Fe/Zr multilayers with the constant Zr layer thickness of 2 nm

The significant coercivity drop is evident at a critical Fe thickness of about 2.3 nm. This change is explained by a structural transition from the polycrystalline phase with high coercivity to the soft magnetic nanocrystalline phase with a grain size lower than the magnetic exchange length (about 15 nm). Similar situation was observed in Co/Zr and Co/Ti multilayers with the Zr(Ti) critical thickness of about 3 nm.

4. MECHANICAL PROPERTIES

4.1. Superhardness

Connections between nanoscale structure and mechanical properties for metals, alloys, intermetallics, ceramics, and polymers including nanocomposites play important role in the development of new materials with the high characteristics of strength, ductility, superplasticity, fracture toughness, and thermo-mechanical stability. This is very comprehensive problem and there are more than several hundreds papers and many books/proceedings/reviews on this topic. So our attention will be concentrated only in limited scope such as some considerations on superhardness, ductility, and superplasticity of intrinsic brittle NM-based carbides, nitrides, borides, and so on, because the metallic NM mechanical properties have been described in many sources (see, e.g., some recent of them [87-92]).

Aforesaid high-melting point compounds are typical brittle solids which are deformed without residual plastic deformation. They are characterized by high values of hardness (up to Vickers microhardness H_V=20-40 GPa) that can be increased by decreasing of grain size The boundary between hard materials and superhard ones is very conditional and it is assumed that the

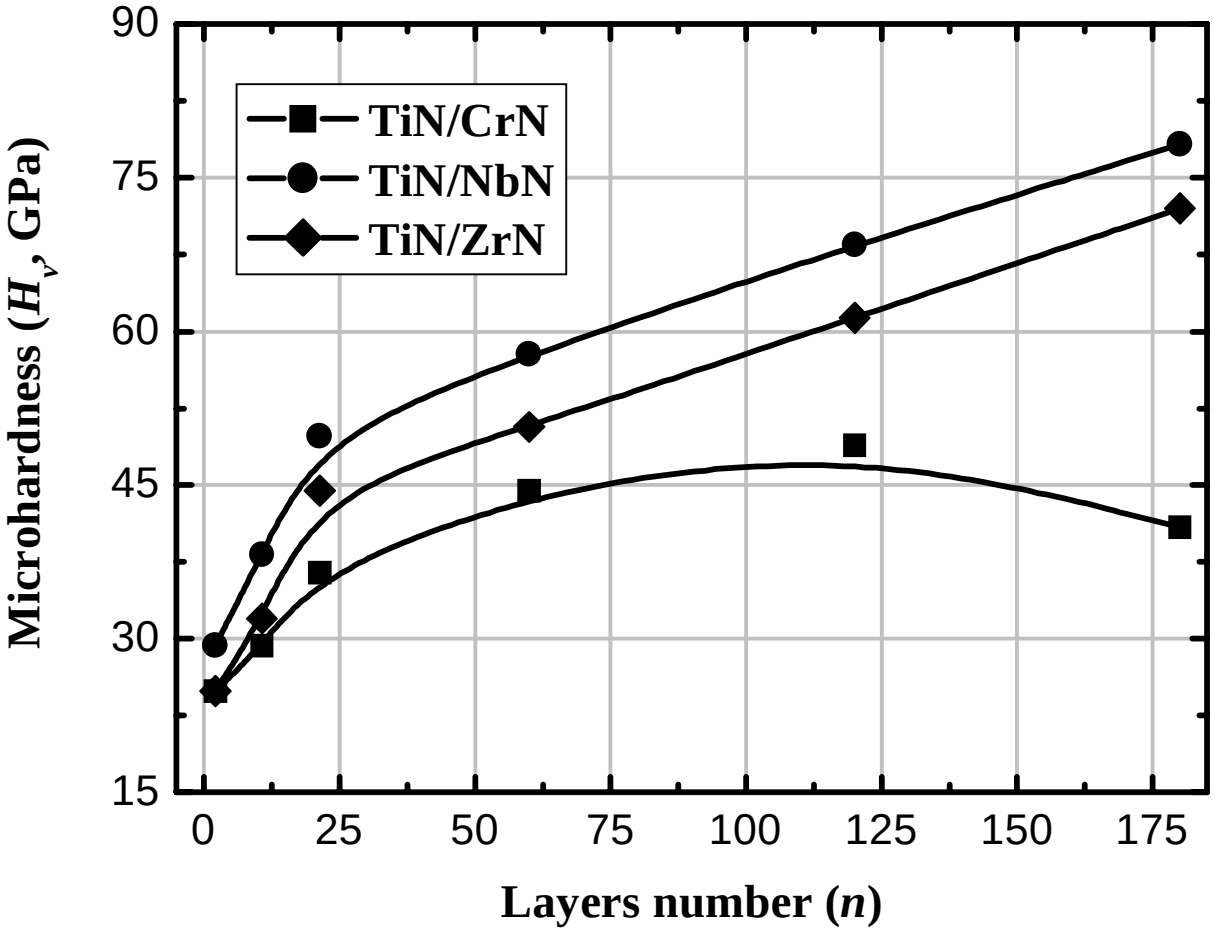

Fig. 9. Influence of the number of layers on the nitride film hardness, data from [108].

superhardness values are more than ~50 GPa. Beginning from 1987-1990, there are extensive studies of new superhard materials-based high-melting point compounds (see, e.g., some comprehensive reviews [51,93-100] and book [101]). The concept of hard multilayered films was formulated in 1986 [102].

Table 6 contains the first results on the superhard materials which have been independently studied by the USA/Sweden, Russian, German, and Austrian researches in both multilayer nitride films and monolayer boride films [98].

The hardness values in Table 6 are about 1.5-4 times higher then the values for *cg* TiB_2, TiN, and other high-melting point compounds with conventional structure; that is the nanostructure effect result. This is especially obvious in the case of multilayered nitride films. Fig. 9 shows the microhardness of the TiN/ZrN, TiN/NbN, and TiN/CrN multilayered films as a function of the layer number for films with a similar total thickness of nearly 2 μm [107,108].

It can be seen from Fig. 9 that for the TiN/NbN and TiN/ZrN films with ~180 layers number (i.e., monolayer thickness ~ 10 nm), the hardness is about 70-80 GPa, i.e. approximately that of diamond. The different behavior of TiN/CrN is connected with (Ti,Cr)N solution formation for more than 100 layers which has been shown by XRD analysis. This observation also confirms that interphase boundaries and layer lattice mismatch are the main factors influenced the hardness increase. However, it is necessary to point that there are at least four physical reasons for the observed increase in the film hardness: (i) interphase boundaries stop dislocation motion or crack propagation; (ii) the crystallites inside the monolayers have a low size (equal to, close to or smaller than the layer thickness); (iii) the dislocation density increases as a result of the layer lattice mismatch; and (iv) a

Table 6. Some first results for superhard films [98].

Films	Hardness H_V (GPa)	Year	Authors
Monolayer films			
$Ti(B,C)_X$	~ 70	1990	Knotek *et al.* [103]
$Ti(B,N)_X$	~ 60	1990	Mitterer *et al.* [104]
a-B_4C	50-70	1992	Veprek [105]
Multilayer films			
TiN/VN	54	1987	Helmerson *et al.* [106]
TiN/NbN	~50; ~78	1991, 1992	Andrievski *et al.* [107,108]
TiN/NbN	48	1992	Shinn *et al.* [109]
TiN/ZrN	~44; ~70	1991, 1992	Andrievski *et al.* [107,108]

more favorable situation exists with the residual compression stresses in multilayer films as compared with monolayer those (see, for example, the residual compression stresses in the TiN and TiAlN/VN films [110]).

Some new results on high values of hardness could be mentioned. Very high mechanical properties have been observed in the case of a five-nanolayered cubic boron nitride/diamond structure (with each layer a thickness of ~100 nm): the hardness value of 82 GPa and the elastic modulus in the range of 800-900 GPa [111]. As applied to TiN/Si_3N_4 and TiN/Si_3N_4/$TiSi_2$ nanocomposite films, the ideal shear strength of a variety TiN/SiN_X/TiN interfaces have been calculated with the *ab initio* density functional method [112]. These calculations approved the high hardness values of > 105 GPa, which had been observed early. Interesting combination of high hardness and Young modulus values (66.4 GPa and 510 GPa respectively) with the high elastic recovery (83.3%) has been realized in the case of nanocomposite film (TiC nanoinclusions in amorphous carbon matrix) prepared by dual plasma technique [113]. The important synergetic potential of (Ti,Al,Cr,Si,Y)N film to adapt in operating extreme conditions and improve the wear behavior is demonstrated in paper [114]. This list can be continued, but it is clear that above mentioned high level properties depend not only from the grain size but also from the interface state and in this connection the role of technology is very important.

It should be noted that success in preparing superhard bulk NM using conventional powder technology is modest compared with nanostructured films. The main difficulty in this route is a retention of the nanocrystalline structure with full densification. Therefore, until the present day, both single-phase bulks and composites prepared have a grain size not less than ~50 nm and with some residual porosity, that results in the hardness values of <50 GPa [115]. Only high pressure/high temperature technique (pressure of 16-20 GPa and T=1800-1900K) as applied to boron nitride resulted in the hardness value of 85 GPa [116]. It worth to point that the high pressure/high temperatures synthesis of BN nanocomposites with high fracture toughness and hardness values (K_{IC}=15-18 MPa $m^{0.5}$ and H_V~80 MPa) was described in former USSR about 30 years ago (tool material on trade "Heksanit R") [117]. Nevertheless, the recent results [116] seem to be also very important because they specify the hardness SDE. This maximum value was observed in specimens having two-phase nanostructure (hexagonal and cubic modifications) with the grain size of 14 nm. Fig. 10 shows the hardness change as a function of the crystalline size [116].

It is interesting that the availability of the hardness non-monotonous change both in the case of the BN nanocomposite and cubic BN (so-called the inverse Hall-Petch behavior). It is assumed that the great hardness increase for nanocomposite specimens is due to the combination of the Hall-Petch and the quantum confinement effects. The last one is proposed to consist in a semi-empirical theory of the covalent crystal hardness [118].

4.2. Ductility and superplasticity

A general overview of key concepts on the NM ductility/superplasticity was presented in review [119]. The deformation mechanism specific features of these phenomenona are discussed such

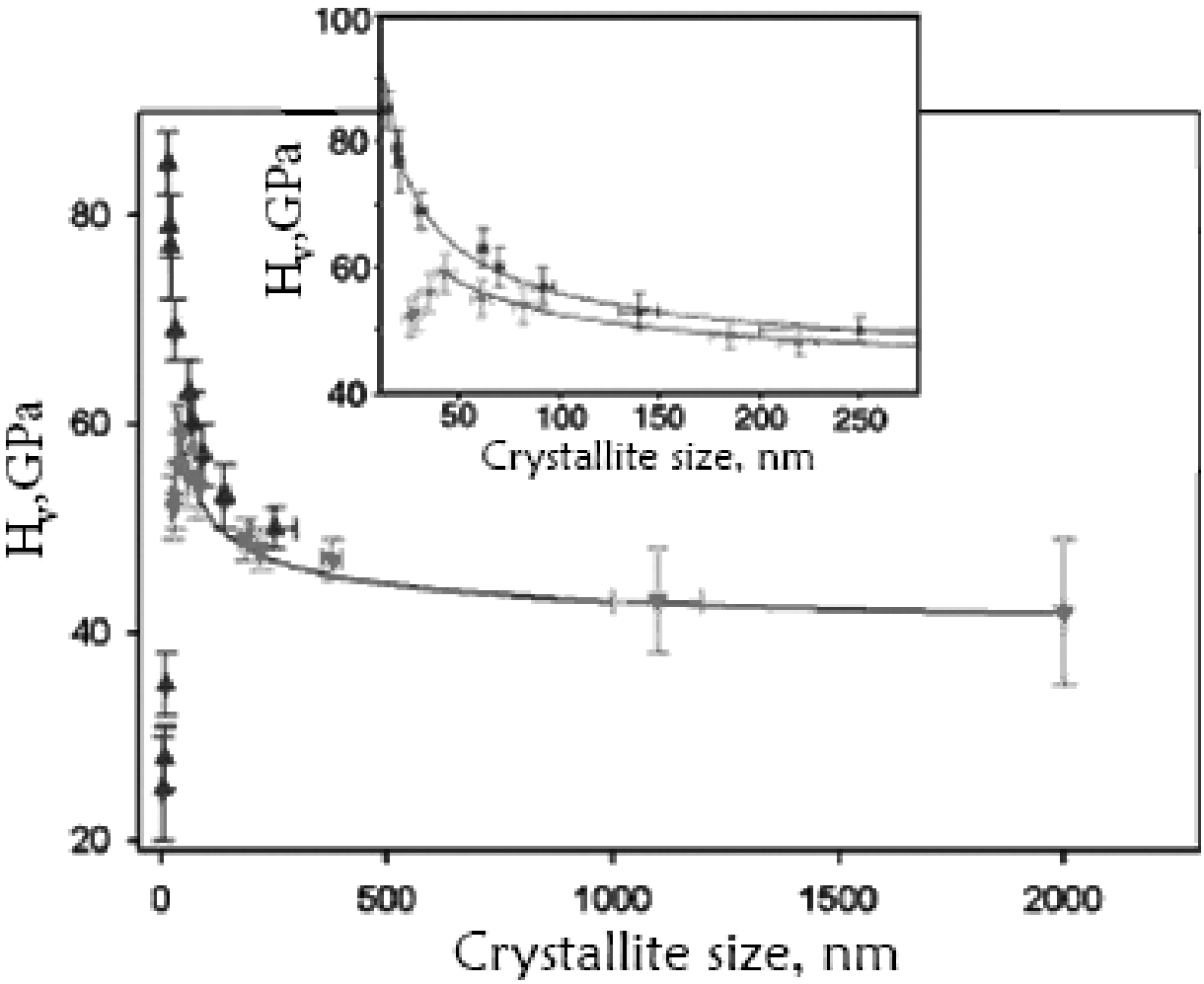

Fig. 10. Vickers hardness (H_V) as a function of the crystalline size. Triangles correspond to the data of aggregated BN composites; inversed triangles, cubic BN (and lower curve in inset), replotted from [116].

as the dislocation slip, grain boundary sliding, grain boundary diffusional creep, rotation deformation, triple junction creep, and so on. Superplasticity is usually defined as the ability of a material to exhibit a large degree of elongation prior to its failure, typically larger than 200%. This definition is formulated for deformed metals and alloys. As applied to hard-deformed and brittle solids, the deformation can be in other forms such as compression. In spite of the nitride/carbide intrinsic brittleness, there are some examples of ductility and superplasticity of these subjects at nanoscale size.

Fig. 11 shows a typical fully dense columnar nanostructure of a TiN film after load indentation [93,120].

The example of residual plastic deformation of brittle TiN columns (with the width of around 200-300 nm) in conditions of non-uniform compression is evident and very impressive. Inside these columns, there are nanocrystallites with a size about 10 nm and lattice dislocations observed by HRTEM inside them [121]. The crossover of many deformation mechanisms during indentation of nano-SiC has been recorded by multimillion-atom molecular dynamics simulation [122]. These deformation mechanisms are cooperative grain sliding, grain rotations, and intergranular dislocation formation similar to stick-slip behavior. However, ductile deformation of brittle intrinsic NM (films and bulks) induced by lattice dislocation slip is observed very seldom, more often brittle fracture and cleavage are reported [89,90,92]. This behavior is a result of the effect of nanocracks that are originated along GB and near TJ by both deformation process [89,90] and incomplete technology.

Recently the plastic deformation availability in β-SiC single-crystal nanowires (diameter of 50-100 nm) has been fixed *in-situ* SEM and TEM experiments [123,124]. The dislocation density increase at an initial stage and amorphization in final one have been observed; the primary slip system was {111}<110> as it is in the case of ordinary FCC subjects. Bending and tensile deformation at temperatures close to room temperature was very large (about 200% and more) and has never been observed in conventional bulk SiC *cg*-materials in which the brittle-ductile transition temperature (BDTT) is about 900-1200 °C [125]. Then the SDE contribution to the BDTT decrease is very significant.

The realization the BDTT low value in nanoceramics is not so easy due to difficulties in preparation of defect-free and fully dense nanobulks. Only using spark plasma sintering of ultrafine nanoparticles results in the representative specimen preparation, see the case of nanostructured MgO with the average grain size of 37±17 nm reported in [126]. Fig. 12 shows typical stress-strain curves of nano-MgO and *cg*-MgO in compression at different temperatures.

It is evident that all fully dense MgO nanoceramics at temperatures as low as 700 °C ($0.31T_m$) exhibit elastic perfectly plastic behavior with no strain hardening. At the same time, *cg* specimen (curve 800 °C) exhibits brittle behavior under compression at 800 °C. The nanostructure effect is very impressive on the BDTT decrease with revealing superplasticity. The homologous temperatures of these experiments were very low and seem to be the lowest ever observed for superplastic deformation of ceramics.

As applied to intermetallic Ni_3Al, the transition to nanospecimens (as-processed by severe plastic deformation with grain size of around 50 nm) was found to be superplastic at a temperature 450 °C below the superplastic temperature in the microcrystalline regime [127]. A forming temperature higher than $0.5T_m$ is generally considered as a necessary condition for conventional superplasticity. The strain rate ($\dot{\varepsilon}$) relation for superplastic flow can be expressed in general in the following form

$$\dot{\varepsilon} = A\frac{DGn}{kT}\cdot\frac{b^m}{L^m}\cdot\frac{\sigma_f^p}{G^p}, \qquad (17)$$

where A is a material constant, D is the coefficient of GB diffusion, G is the shear modulus, b is the Burgers vector, k is the Boltzmann's constant, σ_f is the flow stress, p and m are the stress and grain size exponents (for superplastic materials p and m are typically between 1 and 3). It is obvious that the small L value objects (i.e. nanostructures) are very attractive for the superplasticity realization such as net-shape forming and joining of materials. On the other side, the superplastic deformation of components at the work conditions is inadmissible.

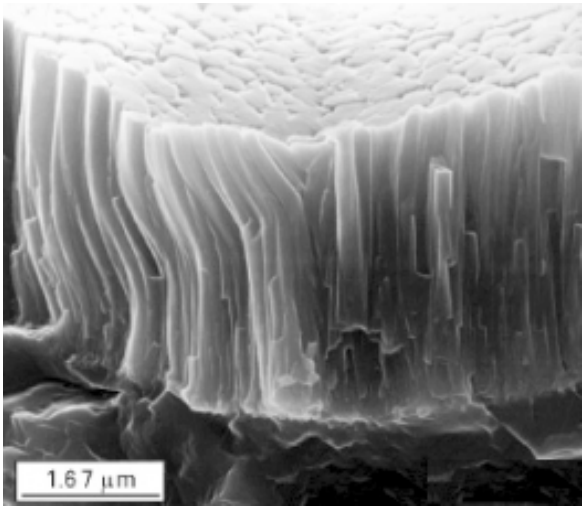

Fig. 11. High resolution SEM image of a fractured cross-section of TiN film by indentation imprint, replotted from [120].

An analysis of creep tests [126] performed at different stresses and temperatures reveals in the stress exponent p = 2±0.1 and the activation energy Q = 202±9 kJ/mol (relationship (17)). The HRSEM nanostructure study prior to and after the plastic deformation at 800 °C have not revealed the form/size grain change. These data and the detail discussion of the mechanisms, controlling the observed superplasticity, resulted in conclusions that dislocation activity should be discarded and mutual sliding of nanometer grains and atomic transport along their boundaries play the dominant role. Authors [126] suggested two general and quite evident conditions that must be fulfilled to accomplish low-temperature superplasticity in ceramics. The first is that the grain size must be small enough to allow grains to reach a significant mobility. The second is that ionic diffusion processes must be active enough to accommodate plasticity into stationary regimes with no microstructural evolution. However, the more precise specifications as applied to the different NM nanostructure must be studied.

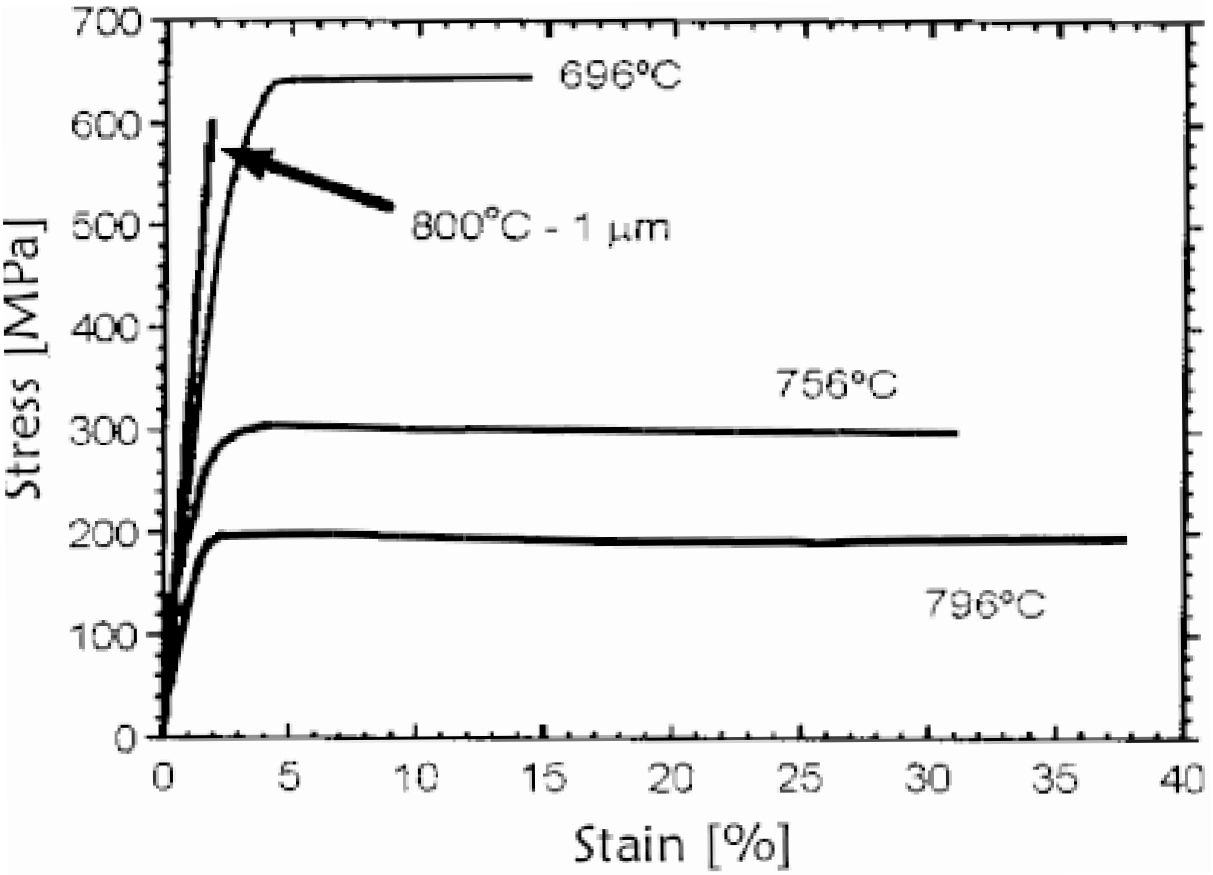

Fig. 12. Stress-strain curves recorded by compression for the MgO nanocrystalline (*L*~37 nm) and coarse-grained (A; *L*~1 μm) specimens at strain-rate of $2x10^{-5}s^{-1}$ and at different temperatures, replotted from [126].

The compression test of nanosized β - Si_3N_4 ceramics (with sintering aid of 5 mol.%Y_2O_3 + 2 mol.%Al_2O_3 for liquid phase formation; the grain size of 68 nm) revealed the existence of two deformation regions in terms of the stress exponent (*p*), grain size one (*m*), and activation energy (*Q*) [128]. At comparatively low stresses (<10-40 MPa), deformation is characterized by *p*~2, *m*~1.1, and *Q*~858 kJ/mol, whereas at stresses higher than 10-40 MPa (in function of temperature) deformation is characterized by *p*~1, *m*~2.6, and *Q*~572 kJ/mol. Concurrent grain growth was observed during deformation, but recrystallization was not accompanied by obvious strain hardening because of the strong texture developed. The respectively superplastic deformation is considered at first region to be occurred by an interface-controlled solution-precipitation process, whereas the GB sliding process accommodated by diffusion-controlled solution precipitation plays a dominant role in second region.

In addition to the Si_3N_4-based NM superplasticity, it seems to be interesting to remind results on creep rate in the system of Si_3N_4-TiB_2 because these specimens have been prepared by hot consolidation at high pressure without sintering aid (*T* = 1800 °C and pressure of 4 GPa). The porosity of specimens was of 1-3% [129]. Fig. 13 shows the creep rate concentration change in this system for two types of specimens prepared from ultrafine Si_3N_4 powders and *cg* counterparts.

It can be seen that for composition with 25 vol.% Si_3N_4, the maximum creep rate (the whole deformation was about 30%) was fixed. This anomaly (which can be considered as a superplasticity revealing) was displayed only when the Si_3N_4 ultrafine powders were used and their grain size in hot-consolidated specimens was near 500 nm (the TiB_2 grain size was about 2 μm). Experiments also demonstrated that in a power law $\dot{\varepsilon} \sim \sigma_f^p$ the stress exponent was about 2 that agree with results [128].

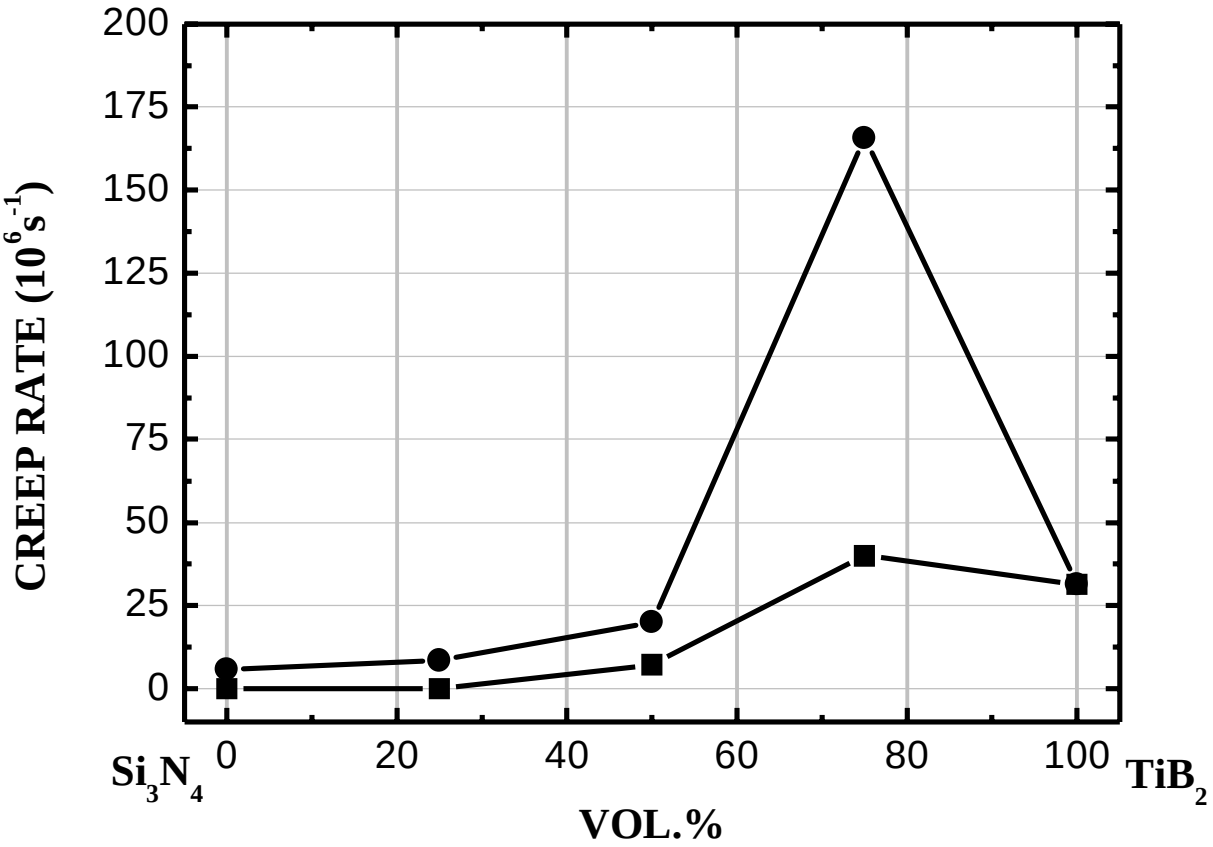

Fig. 13. Creep rate change in the system Si_3N_4-TiB_2 (T=1600 °C, t=30 min, stress of 20 MPa). (■) – curve for specimens prepared from mixed powders with particle size of 2-4 μm; (●) – curve for specimens prepared from mixed powders with particle size of 0.5 μm (Si_3N_4) and of 2-4 μm (TiB_2), data from [129].

As applied to revealing superplasticity, dual nanocomposites have some preference because of slow recrystallization. The superplasticity behavior has been fixed in many two-phase composites such as TiC-ZrC, TiC-TiB_2, TiC-C, TiC-VC, VC-HfC, ZrB_2-ZrN, AlN-Y_2O_3, ZrB_2-ZrC, and so on [124,130]. However, the grain size in these experiments was not in nanointerval and the temperatures of revealing superplasticity were very high. The detail discussion of a high-strain-rate superplasticity in one-, two-, and three-phase oxide ceramics is presented in review [131]. ZrO_2-, Al_2O_3-, MgO-, and TiO_2-based nanocomposites are fully characterized both applied processing dependence, creep equation, cavity nucleation, dynamic grain growth, and other aspects of superplasticity. Now there are nanocomposites-based ZrO_2(3Y) and spinel+Al_2O_3 which have high values of strain-rate superplasticity ($\dot{\varepsilon}$ ~0.1-1 s^{-1} and large tensile deformation of 390-2500% at 1500-1650 °C; with an average grain size of 300-450 nm). A fully dense specimens consisting of ZrO_2+Al_2O_3+$MgAl_2O_4$ (40/30/30 vol.%; the grains are approximately 100 nm in size), prepared by spark plasma sintering, were deformed at 1150 °C at a strain rate of the order of 10^{-2} s^{-1} [132]. This is an example of superplastic forming of ceramic nanocomposite at a commercially attractive temperature of 1150 °C and at high-strait-rate conditions.

Small additions of BN nanotubes (0.5-2.5 wt.%; an average diameter of 60 nm and a length over several tens of micrometer) are shown to produce a considerable effect on enhancing superplasticity of Al_2O_3/SiC ceramics [133]. Fig. 14 shows the effect of BN nanotubes and powder additions on high-temperature deformation of alumina and silicon carbide.

It is obvious that small additions of BN nanotubes significantly enhance the high-temperature deformation of these brittle subjects. Thus, in the case of pure Al_2O_3 (the grain size of around 3 μm), brittle fracture (point 'X' at Fig. 14a) convert to superplasticity deformation as applied to the (Al_2O_3+BN) microcomposites (the average grain

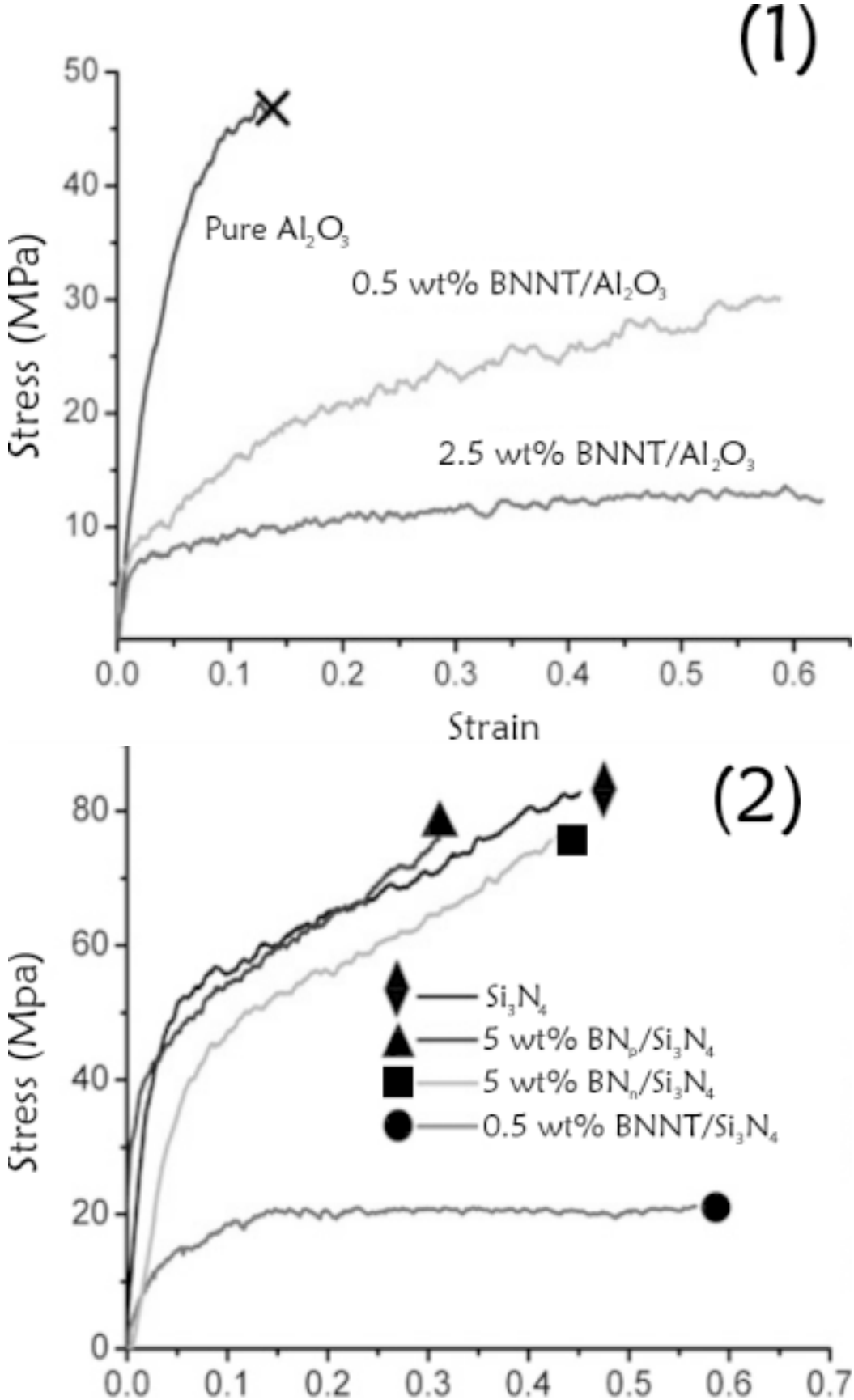

Fig. 14. Stress–strain curves of pure alumina / BNNT composites at 1450 °C (1) and of Si_3N_4 composites doped with different BN materials at 1500 °C (2). BNNT – BN nanotube; BN_P – micro-sized powder; BN_N – nano-sized powder (average particle size ~ 80 nm. All deformations were conducted at a constant strain rate of 1 10^{-4} s^{-1}, replotted from [133].

size of around 600 nm). It is also interesting that this dramatic effect reveals only in the nanotube additions and does not observe in the case of conventional and nanocrystalline BN powders (Fig. 14 panel (2)).

It is necessary to point that now there are many interesting and encouraging experimental results in the field of ductility/superplasticity of brittle NM-based high-melting point compounds. However, detailed and systematic information on grain size effect is not so comprehensive and in most cases is exhausted by comparison of the strain rate in the *cg* and nanostructured states. It is difficult to indicate the real mechanism of deformation from this scanty information. In this connection it seems very reasonable to study the superhardness/superplasticity features in a wide temperature and nanosize interval using one and the same subject. These results could elucidate the evolution and transition of interfaces from dislocation stopors to medium making easy deformation. Further theoretical and experimental studies are needed in order to develop optimal regimes of high-strain-rate-forming technology suitable for ceramic nanomaterials.

5. CONCLUSIONS

In this review, an attempt has been made to analyze the current progress in the studying and understanding of SDE for the NM properties. In some cases the large body of information and limited space forced only to point and consider problems, as it was from bird's flight, without comprehensive analysis. Nevertheless, it is clear from the foregoing that only first steps have been taken in the field of the SDE questions. There are a lot of unresolved aspects that have been pointed to earlier. In many cases we can not predict the size effects. It must be noted also that the nanostructure versions are very numerous (for example, there are 12 types of nanostructures [134] or even 36 ones [135]) but in the SDE problems only very simple ordinary examples are analyzed and the stereological concept development on various nanosructures seems to be very important. A better understanding of the SDE various aspects is needed in order to realize full potentials of NM and nanotechnology.

ACKNOWLEDGEMENTS

The author should like its appreciation to Profs. M. Mayo, H. Gleiter, A. Glezer, K. Lu, C. Mitterer, S. Veprek, and J. Weissmuller for fruitful discussions and papers sending as well as Drs. G. Kalinnikov and A. Khatchoian for their effective help. This research is supported by the Russian Basic Research Foundation (Projects No 08-03-00105) and the Fundamental Problem Program of Russian Academy of Sciences (parts P-18 and P-27).

REFERENCES

[1] R.A. Andrievski and A.M. Glezer // *Phys. Met. Metallogr.* **88** (1999) 45 (English transl.).
[2] R.A. Andrievski and A.M. Glezer // *Phys. Met. Metallogr.* **89** (2000) 83 (English transl.).
[3] R.A. Andrievski and A.M. Glezer // *Scr. Mater.* **44** (2001) 1621.
[4] R.A. Andrievski and A.V. Ragulya, *Nanostructured Materials* (Publishing Center "Academia", Moscow, 2005), In Russian.
[5] R.A. Andrievski // *Mater. Sci. Forum* **494** (2005) 113.
[6] E. Arzt // *Acta Mater.* **46** (1998) 5611.
[7] J. Weissmuller, In: *Nanocrystalline Metals and Oxides: Selected Properties and Applications*, ed. by P. Knauth and J. Schonman (Kluwer Academic Publishers, Boston, 2001), p.1.
[8] J. Weissmuller, In: *Proc. of the 22nd Riso International Symposium on Materials Science: Science of Metastable and Nanocrystalline Alloys. Structure, Properties and Modelling*, ed. by A.R. Dinesen, M. Eldrup, D.E. Jensen, S. Linderoth, T.B. Pederson, N.H. Pryds, A. Pedersen and J.A. Wert (Riso National Laboratory, Roskilde, Denmark, 2001), p.155.
[9] P. Buhler, *Nanothermodynamics* (Yanus, St. Petersburg, 2004), In Russian.
[10] A.I. Gusev, *Nanomaterials, Nanostructures, Nanotechnologies* (Fizmatlit, Moscow, 2005), In Russian.
[11] A.I. Rusanov // *Surf. Sci. Rep.* **58** (2005) 111.
[12] U. Tartaglino, T. Zykova-Timan, F. Ercolessi and E. Tossati // *Phys. Rep.* **411** (2005) 291.
[13] I.P. Suzdalev, *Nanotechnology: Physics and Chemistry of Nanoclusters, Nanostructures and Nanomaterials* (KomKniga, Moscow, 2006), In Russian.
[14] A.I. Rusanov // *Colloid J.* **68** (2006) 334 (English transl.).
[15] G.B. Sergeev, *Nanochemistry* (Elsevier, Amsterdam-Boston, 2006).
[16] E. Roduner, *Nanoscopic Materials. Size-Dependent Phenomena* (RSC Publishing, Cambridge, 2006).

[17] A.V. Ragulya and V.V. Skorokhod, *Consolidated Nanostructured Materials* (Naukova Dumka, Kiev, 2007), In Russian.
[18] G. Wilde, P. Bunzel, H. Rozner and J. Weissmueller // *J. All. Comp.* **434** (2007) 276.
[19] Q.S. Mei and K. Lu // *Progr. Mater. Sci.* **52** (2007) 1175.
[20] M.N. Magomedov // *Phys. Sol. State* **46** (2004) 954 (English transl.).
[21] V.M. Samsonov // *Bull. Russ. Acad. Sci. Phys. Ser.* **69** (2005) 1161 (English transl.).
[22] G. Ouyang, X. Tan and G. Yang // *Phys. Rev.* B **74** (2006) 195408.
[23] S. Rekhviashvili, E.V. Kishtikova, R.U. Karmokova and A.M. Karmokov // *Techn. Phys. Lett*. **33** (2007) 48 (English transl.).
[24] A. Schroder, J. Fleig, H. Drings and R. Wuerschum // *Sol. State Ionics* **173** (2004) 95.
[25] K.K. Nanda, A. Maisels, F.E. Kruis, H. Fissan and S. Stappert // *Phys. Rev. Lett.* **91** (2003) 106102.
[26] A. Caro and H. Van Swygenhoven // *Phys. Rev.* B **63** (2001) 134101.
[27] K. Lu and N.X. Sun // *Phil. Mag. Lett*. **75** (1997) 389.
[28] G. Ouyang, L.H. Liang, C.X. Wang and G.W. Yang // *Appl. Phys. Lett*. **88** (2006) 091914.
[29] J.M. Howe, A.M. Mebed, K. Chatterjee, P. Li, M. Murayama and W.C. Johnson // *Acta Mater*. **51** (2003) 1359.
[30] J.G. Lee and H. Mori // *J. Mater. Res.* **20** (2005) 1708.
[31] G. Guisbiers and M. Wautelet M // *Nanotechnology* **17** (2006) 2008.
[32] S. Rekhviashvili and E.V. Kishtikova // *Techn. Phys. Lett.* **32** (2006) 439 (English transl.).
[33] W.H. Qi // *Physica* B **368** (2005) 46.
[34] S. Xiao, W. Hu and J. Yang // *J. Chem. Phys.* **125** (2006) 184504.
[35] D.G. Gromov, S.A. Gavrilov, E.N. Redichev and R.M. Ammosov // *Phys. Sol. State* **49** (2007) 178 (English transl.).
[36] W.H. Qi // *Mod. Phys. Lett.* B **20** (2006) 1943.
[37] A. Suresh, M.J. Mayo and W.D. Poster // *J. Mater. Res.* **18** (2003) 2912.
[38] A. Suresh, M.J. Mayo, W.D. Poster and C.J. Rawn // *J. Am. Ceram. Soc.* **86** (2003) 360.
[39] A.M. Glezer, E.I. Blinova and V.A. Pozdniakov // *Bull. Russ. Acad. Sci. Phys. Ser.* **66** (2002) 1236 (English transl.).
[40] B.Y. Pines and A.I. Bublik // *Doklady AN* **87** (1954) 215, In Russian.
[41] G.B. Thompson, R. Banerjee, S.A. Dregia and H.L. Fraser, In: *Nanostructured Interfaces*, ed. by J.M. Plitzko, G. Duscher, Y. Zhu and H. Ichinose (MRS, Warrendale, v. 727, 2002), p. R5.8.
[42] W.A. Jesser, R.Z. Shneck and W.W. Gile // *Phys. Rev.* B **69** (2004) 144121.
[43] V.V. Danilenko // *Comb. Expl. Shock Waves* **41** (2005) 460 (English transl.).
[44] R.A. Andrievski and G.V. Kalinnikov // *Glass Phys. Chem.* **33** (2007) 344 (English transl.).
[45] G.V. Kalinnikov, R.A. Andrievski, V.N. Kopylov and D. Louzguine // *Phys. Sol. State* **50** (2008) 374 (English transl.).
[46] R.A. Andrievski // *Mater. Sci. Forum* **555** (2007) 327.
[47] R.A. Andrievski // *Physics-Uspekhi* **50** (2007) 691 (English transl.).
[48] G.A. Dorofeev and E.P. Elsukov // *Phys. Met. Metallogr.* **103** (2007) 593 (English transl.).
[49] G. Ouyang, X. Tan, C.X. Wang and G.W. Yang // *Nanotechnology* **17** (2006) 4257.
[50] R.A. Andrievski and G.V.Kalinnikov // *Surf. Coat. Technol.* **142-144** (2001) 573.
[51] R.A. Andrievski // *J. Mater. Sci.* **29** (1994) 614.
[52] V.M. Koshkin and V.V. Slezov // *Techn. Phys. Lett.* **30** (2004) 367 (English transl.).
[53] A.S. Shirinyan, A.M. Gusak and M. Wautelet // *Acta Mater.* **53** (2005) 5025.
[54] Y.N. Gornostyrev, I.K. Razumov and A.E. Yermakov // *J. Mater. Sci.* **39** (2004) 5003.
[55] P.H. Mayrhofer, F.D. Fisher, H.J. Bohm, C. Mitterer and J.M. Schneider // *Acta Mater.* **55** (2007) 1441.
[56] F. Huang, Y. Tong and Sh. Yun // *Phys. Sol. State* **46** (2004) 616 (English transl.).
[57] J. Weissmuller, P. Bunzel and G. Wilde // *Scr. Mater.* **51** (2004) 813.
[58] M.G. Zemlianov, G.Ch. Panova, G.F. Syrych and A.A. Shikov // *Phys. Sol. State* **47** (2005) 362 (English transl.).
[59] M.G. Zemlianov, G.Ch. Panova, G.F. Syrych and A.A. Shikov // *Phys. Sol. State* **48** (2006) 139 (English transl.).
[60] S. Bose, P. Raychadhuri, R. Banerjee and P. Ayyub // *Phys Review* B **74** (2006) 224502.
[61]. S. Bose, P. Raychadhuri, R. Banerjee, P. Vasa and P. Ayyub// *Phys. Rev. Lett.* **95** (2005) 147003.

[62] V.N. Troitskiy, I.A. Domashnev, E.N. Kurkin, O. M. Grebtsova, V. I. Berestenko, I. L. Balikhin and S. N. Gurov // *J. Nanopart. Res.* **5** (2003) 521.
[63] M.N. Magomedov // *Phys. Sol. State* **45** (2003) 1213 (English transl.).
[64] X.Y. Lang and Q. Jiang // *Sol. St. Commun.* **134** (2005) 797.
[65] C. Demetry and X. Shi // *Sol. State Ionics* **118** (1999) 271.
[66] X. Guo and X. Zhang // *Acta Mater.* **51** (2003) 2539.
[67] I. Kosacki, Ch. M. Rouleau, P.B. Becher, J. Bentley and D.H. Lowndes // *Sol. State Ionics* **176** (2005) 1319.
[68] Y.-M. Chiang, E.B. Lavik and D.A. Bloom // *Nanostruct. Mater.* **9** (1997) 633.
[69] P.S. Manning, J.D. Sirman, R.A. DeSouza and J.A. Kilner // *Sol. State Ionics* **100** (1997) 1.
[70] M.D. Glinchuk, P.I. Bykov and B. Khilcher // *Phys. Sol. State* **48** (2006) 2199 (English transl.).
[71] P. Chiu and I. Shih // *Nanotechnology* **15** (2004) 1489.
[72] D.V. Fedorov, P. Zahn and L. Mertig // *Thin Solid Films* **473** (2005) 346.
[73] D.F. Urban, J. Burki, C.A. Stafford and H. Grabert // *Phys. Rev.* B **74** (2006) 245414.
[74] E. Shapira, A. Tsukernik and Y. Selzer // Nanotechnology **18** (2007) 485703.
[75] R.A. Andrievski, Z.M. Dashevsky and G.V. Kalinnikov // *Techn. Phys. Lett.* **30** (2004) 930 (English transl.).
[76] H.-R. Yang, G.-R. Bai, L.J. Thompson and J.A. Eastman // *Acta Mater.* **50** (2002) 2309.
[77] G. Chen, A. Narayanaswamy and C. Dames // *Superlatt. Microstr.* **35** (2004) 161.
[78] O.G. Vendik, N.Y. Medvedeva and S.P. Zubko // *Techn. Phys. Lett.* **33** (2007) 231 (English transl.).
[79] X.Y. Lang and Q. Jiang // *J. Nanopart. Res.* **9** (2007) 595.
[80] Y.N. Ovchinnikov // *J. Exper. Theor. Phys.* **104** (2007) 254 (English transl.).
[81] G.N. Frolov // *Techn. Phys.* **49** (2004) 895 (English transl.).
[82] W.H. Zhong, Ch.Q. Sun and S. Li // *Sol. State Comm.* **130** (2004) 603.
[83] V.M. Fedosyuk // *Nanostrukturnoe Materialovedenie* **2-6** (2005) 3, In Russian.
[84] L. Smardz // *J. All. Comp.* **395** (2005) 17.
[85] D. Rafaja, L. Havela, R. Kuzel, F. Wastin, E. Colineau, T. Gouder // *J. All. Comp.* **386** (2005) 87.
[86] R.A. Andrievski // *Mater. Sci. Forum* **518** (2006) 9.
[87] M.A. Meyers, A. Mishra and D.J. Benson // *Progr. Mater. Sci.* **51** (2006) 427.
[88] E. Ma // *JOM* **58** (2006) 49.
[89] C.C. Koch, I.A. Ovid'ko, S. Seal and S. Veprek, *Structural Nanocrystalline Materials: Fundamentals and Applications* (Cambridge University Press, Cambridge, 2007).
[90] I.A. Ovid'ko // *J. Mater. Sci.* **42** (2007) 1694.
[91] R.Z. Valiev and I.V. Aleksandrov, *Bulk Nanostructured Metallic Materials: Preparation, Structure and Properties* (Akademkniga, Moscow, 2007), In Russian.
[92] R.A. Andrievski and A.M.Glezer // *Physics – Uspekhi* **52** (2009) 315.
[93] R.A. Andrievski // *J. Mater. Sci.* **32** (1997) 4463.
[94] S. Veprek // *J. Vac. Sci. Technol.* A **17** (1999) 2401.
[95] R.A. Andrievski // *Int. J. Refr. Met. Hard Mater.* **19** (2001) 447.
[96] G.M. Demyashev, A.L. Taube and E. Siores, In: *Encyclopedia of Nanoscience and Nanotechnology*, ed. by H.S. Nalwa (Amer. Sci. Publ., USA, v. 10, 2004), p. 191.
[97] P.H. Mayrhofer, C. Mitterer and H. Clemens // *Adv. Eng. Mater.* **7** (2005) 1071.
[98] R.A. Andrievski // *Surf. Coat. Technol.* **201** (2007) 6112.
[99] S. Veprek and M.G.J. Veprek-Heijman // *Surf. Coat. Technol.* **201** (2007) 6064.
[100] G. Abadias, A. Michel and C. Tromas // *Surf. Coat. Technol.* **202** (2007) 844.
[101] A. Cavaleiro and J.Th.M. De Hosson (Eds.), *Nanostructured Coatings* (Springer, New York, 2006).
[102] H. Holleck // *J. Vac. Sci. Technol.* A **4** (1986) 2661.
[103] O. Knotek, R. Breidenbach, F. Jungblit and F.L. Lofler // *Surf. Coat. Technol.* **43-44** (1990) 107.
[104] C. Mitterer, M. Rauter and P. Rodhammer // *Surf. Coat. Technol*. **41** (1990) 351.
[105] S. Veprek // *Plasma Chem. Plasma Process*. **12** (1992) 219.
[106] U. Helmerson, S. Todorova, S.A. Barnett, J.E. Suundgren, I.C. Market and J.E. Greene // *J. Appl. Phys.* **62** (1987) 481.

[107] R.A. Andrievski, I.A. Anisimova and V.P. Anisimov // *Thin Sol. Films* **205** (1991) 171.
[108] R.A. Andrievski, I.A. Anisimova and V.P. Anisimov // *Fizika i Chimia Obrabotki Materialov* **N2** (1992) 99, In Russian.
[109] M. Shinn, L. Hultman and S.A. Barnet // *J. Mater. Res.* **7** (1992) 99.
[110] W.D. Munz // *MRS Bull.* **28** (2003) 173.
[111] H.Q. Li, K.M. Leung, K.L. Ma, Q. Ye, Y.M. Chong, Y.S. Zou, W.J. Zhang, S.T. Lee and I. Bello // *Appl. Phys. Lett.* **91** (2007) 201918.
[112] S. Veprek, A.S. Argon and R.F. Zhang // *Phil. Mag. Lett.* **87** (2007) 955.
[113] Y. Wang, X. Zhang, X. Wu, Q. Li, H. Zhang and X. Zhang // *Mater. Sci. Eng. A* **488** (2008) 112.
[114] G.S. Fox-Rabinovich, S.C. Veldhuis, G.K. Dosbaeva, K. Yamamoto, A.I. Kovalev, D.L. Wainstein, I.S. Gershman, L.S. Shuster and B.D. Beake // *J. Appl. Phys.* **103** (2008) 083510.
[115] R.A. Andrievski, In: *Nanomaterials Handbook*, ed. by Y.G. Gogotsi (CRC Press, Boca Raton, 2006), p.405.
[116] N. Dubrovinskaia, V.L. Solozhenko, N. Miyajima, V. Dmitriev, O.O. Kurakevych and L. Dubrovinsky // *Appl. Phys. Lett.* **90** (2007) 101912.
[117] A.V. Bochko, O.N. Grigor'ev, S.S. Dzhamarov, G.G. Karyuk, A.V. Kurdumov, G.S. Oleinik, A.N. Pilyankevich, V.I. Trefilov, I.N. Frantsevich and A.M. Shatokhin // *Sov. Powd. Metall. Metal. Ceram.* **N10** (1979) 61 (English transl.).
[118] J.S. Tse, D.D. Klug and F. Gao // *Phys. Rev.* B **73** (2006) 140102.
[119] I.A. Ovid'ko // *Rev. Adv. Mater. Sci.* **10** (2005) 89.
[120] K.J. Ma and A. Bloyce // *Surf. Eng.* **11** (1995) 71.
[121] R.A. Andrievski, G.V. Kalinnikov and D.V. Shtanski // *Phys. Solid State* **42** (2000) 760 (English transl.).
[122] I. Szlufarska, A. Nakano and P. Vashishta // *Science* **309** (2005) 911.
[123] X.D. Han, Y.F. Zhang, K. Zheng, X.N. Zhang, Y.J. Hao, X.Y, Guo J. Yuan and Z.L. Wang // *NanoLetters* **7** (2007) 452.
[124] Y. Zhang, X. Han, K. Zheng, Z. Zhang, X. Zhang, J. Fu, Y.Ji, Y. Hao, X. Guo and Z. Wang // *Adv. Funct. Mater.* **17** (2007) 3435.
[125] R.A. Andrievski and I.I. Spivak, *The Strength of High-Melting Point Compounds and Materials on Their Base* (Metallurgia, Cheliabinsk, 1989), In Russian.
[126] A. Dominguez-Rodriguez, D. Gomez-Garcia, E. Zapata-Solvas, J.Z. Shen and R. Chaim // *Scr. Mater.* **56** (2007) 89.
[127] S.X. McFadden, R.S. Mishra, R.Z. Valiev, A.P. Zhilyaev and A.K. Mukherjee // *Nature* **398** (1999) 684.
[128] X. Xu, T. Nishimura, N. Hirosaki, R.-J. Xie, Y. Yamamoto and H. Tanaka // *Acta Mater.* **54** (2006) 255.
[129] R.A. Andrievski, V.T. Ivannikov and V.S. Urbanovich // *Key Eng. Mater.* **89-91** (1994) 445.
[130] R.A. Andrievski, I.I. Spivak and V.V. Klimenko // *Doklady AN* **203** (1972) 279, In Russian.
[131] K. Hiraga, B.-N. Kim, K. Morita, H. Yoshida, T. Suzuki and Y. Sakka // *Sci. Technol. Adv. Mater.* **8** (2007) 578.
[132] D. M. Hulbert, D. Jiang, J.D. Kuntz, Y. Kodera and A.K. Mukherjee // *Scr. Mater.* **56** (2007) 1103.
[133] Q. Huang, Y. Bando, X. Xu, T. Nishimura, C. Zhi, C. Tang, F. Xu, L. Gao and D. Golberg // *Nanotechnology* **18** (2007) 485706.
[134] H. Gleiter // Acta Mater. **48** (2000) 1.
[135] V.V. Pokropivny and V.V. Skorokhod // *Mater. Sci. Eng.* C **27** (2007) 990.